NASA TECHNICAL NOTE

NASA TN D-3675

NASA TN D-3675

C. 1

LOAN COPY: RETURN TO AFWL (WLIL-2) KIRTLAND AFB, N. MEX.

0130669

TECH LIBRARY KAFB, NM

AERODYNAMIC CHARACTERISTICS OF A SERIES OF SPHERICALLY BLUNTED 10° CONES WITH 30° AND 60° BASE FLARES

14 NOV 1966 Technical Library Aerospace Laboratory

by Julius E. Harris

Langley Research Center

Langley Station, Hampton, Va.

NATIONAL AERONAUTICS AND SPACE ADMINISTRATION • WASHINGTON, D. C. • OCTOBER 1966

TECH LIBRARY KAFB, NM
0130699

AERODYNAMIC CHARACTERISTICS OF A SERIES OF SPHERICALLY BLUNTED 10° CONES WITH 30° AND 60° BASE FLARES

By Julius E. Harris

Langley Research Center
Langley Station, Hampton, Va.

NATIONAL AERONAUTICS AND SPACE ADMINISTRATION

For sale by the Clearinghouse for Federal Scientific and Technical Information
Springfield, Virginia 22151 – Price $2.00

AERODYNAMIC CHARACTERISTICS OF A SERIES OF SPHERICALLY BLUNTED 10° CONES WITH 30° AND 60° BASE FLARES

By Julius E. Harris
Langley Research Center

SUMMARY

Force and moment tests have been conducted on a series of 10° semiapex-angle spherically blunted cones with 30° and 60° semiapex-angle base flares in the Langley 11-inch hypersonic tunnel at a Mach number of 9.75 and a Reynolds number based on cone base diameter of 1.56×10^5 for angles of attack from 0° to 45°.

Analysis of the experimental force and moment data from the present investigation indicated that all the configurations were statically stable about a point located on the axis of symmetry one-tenth of a cone base diameter ahead of the centroid of the cone planform area. From schlieren and oil flow studies, the separation induced by the base flares was found to decrease with increasing bluntness ratio for a constant flare angle and to increase with increasing flare angle for a constant bluntness ratio. Agreement between the experimental force and moment coefficients and Newtonian approximations was poor.

INTRODUCTION

The use of pointed or slightly blunted conical bodies is desirable for entry into planetary atmospheres at velocities in excess of earth-escape velocity in order to reduce the total aerodynamic heating. (See refs. 1 and 2.) Radiative heating is much greater than convective heating at these speeds and can be drastically reduced by utilizing entry bodies with highly swept bow shock waves since radiative heating depends on the component of velocity normal to the bow shock wave rather than on the total velocity. These high heating rates will probably cause the cones to undergo significant nose blunting because of ablation. The effects of nose bluntness on the aerodynamic characteristics of slender cones are available in a number of reports. (See refs. 3 to 6.)

The base flare is a possible stabilizing device as well as an aerodynamic drag device for conical entry vehicles. (See ref. 7.) However, at the altitudes accompanying reentry, large flare angles must be used in order to achieve the desired stability and drag characteristics. These flare angles produce large adverse pressure gradients which may

cause the flow to separate ahead of the flare. This separation will in general cause a decrease in flare effectiveness.

The purpose of the present investigation was to obtain the static longitudinal aerodynamic characteristics of a series of 10° semiapex-angle spherically blunted cones with 30° and 60° semiapex-angle base flares. These data, together with oil flow studies, schlieren photographs, and previously published aerodynamic characteristics (ref. 3) were used to determine the effects of bluntness ratio and flare angle on the aerodynamic characteristics as well as to study their effects on separation.

SYMBOLS

A	area
C_A	axial-force coefficient, $F_A/q_\infty A_b$
C_D	drag coefficient, $F_D/q_\infty A_b$
C_L	lift coefficient, $F_L/q_\infty A_b$
C_m	pitching-moment coefficient, $M/q_\infty A_b d$
C_{m_α}	slope of C_m versus α curve, $dC_m/d\alpha$
C_N	normal-force coefficient, $F_N/q_\infty A_b$
C_{N_α}	slope of normal-force coefficient versus α curve, $dC_N/d\alpha$
d	cone base diameter (see fig. 1(a))
D	flare base diameter (see fig. 1(b))
F_A	axial force
F_D	drag force, $F_N \sin \alpha + F_A \cos \alpha$
F_L	lift force, $F_N \cos \alpha - F_A \sin \alpha$
F_N	normal force

l	distance between flow separation point and cone-flare juncture (see fig. 4)
L/D	lift-drag ratio, C_L/C_D
M	pitching moment
M_∞	free-stream Mach number
p	pressure
q	dynamic pressure, $\rho_\infty V_\infty^2/2$
R	Reynolds number $\rho_\infty V_\infty d/\mu_\infty$
r	radius
T	temperature
V	velocity
x	distance between cone-flare juncture and moment reference point on axis of symmetry
$\bar{x}$	axial distance between center of pressure of base flare and cone-flare juncture
α	angle of attack
γ	ratio of specific heats
θ	flare semiapex angle (see fig. 4)
ρ	density
ϕ	cone semiapex angle
ψ	bluntness ratio, r_n/r_b
μ	coefficient of viscosity

Subscripts:

b	base of cone (point at cone-flare juncture)
c	cone
f	flare
n	spherical nose of cone
s	sphere
t	total conditions
∞	free stream
ϕ	value based on cone semiapex angle (see eqs. (1) to (11))
θ	value based on flare semiapex angle (see eqs. (1) to (11))

Model designations:

The model bluntness ratio is designated by I, II, III, and IV and is followed by either 30F or 60F which designates the flare semiapex angle. (See fig. 1.)

TEST FACILITY

The present investigation was conducted in the Langley 11-inch hypersonic tunnel. This facility is designed to operate with air as the test medium for Mach numbers of approximately 7 and 10. Descriptions of the facility are presented in references 8 and 9.

The approximate test conditions for the present investigation are listed in the following table:

γ	7/5
M_∞	9.75
R	1.56×10^5
$p_{t,\infty}$, N/m^2	4.56×10^6
$T_{t,\infty}$, ^oK	950
p_∞, N/m^2	124
T_∞, ^oK	48

INSTRUMENTATION AND ACCURACY OF DATA

An internally mounted strain-gage balance was used in the present investigation to measure the aerodynamic forces and moments. Angles of attack were set during a tunnel run by using a prism mounted in the model flush with the surface to reflect a light beam from a point source outside the tunnel onto a calibrated scale. An ionization gage was used to measure the base pressure. The base pressure drag obtained from these measurements was found to be negligible in comparison to the axial force; consequently, the force coefficient data presented in the present report are not corrected for base pressure drag.

The maximum uncertainties in the force and moment coefficients as determined from static calibration of the strain-gage balance are listed in the following table:

C_N	±0.015
C_A	±0.015
C_m	±0.011

MODELS

The basic model used in the investigation was a 10^o semiapex-angle cone with varying nose bluntness. The bluntness ratio, defined as the ratio of nose radius to base radius, ranged from zero for the sharp cone to 0.763 for the bluntest configuration. The models were fitted with interchangeable 30^o and 60^o semiapex-angle flares. The flare diameter was held constant during the investigation. Drawings of the models are presented in figure 1.

THEORY

Newtonian impact theory estimates of the force and moment coefficients are compared with the experimental data from the present investigation. The tables and equations for spherical caps and right circular cones presented in reference 10 were used to calculate the force and moment coefficients. The basic geometric parameter used in reference 10 was h/a; in the present analysis $h = r_n \cos \phi$ and $a = r_b$. In terms of the bluntness ratio ψ this parameter becomes

$$\frac{h}{a} = \psi \cos \phi \tag{1}$$

The force and moment coefficient equations for spherically blunted cones without base flares in terms of the bluntness ratio and cone semiapex angle (see ref. 3) are as follows:

$$C_N = \left(1 - \psi^2\cos^2\phi\right)C_{N,c,\phi} + \psi^2 C_{N,s} \tag{2}$$

$$C_A = \left(1 - \psi^2\cos^2\phi\right)C_{A,c,\phi} + \psi^2 C_{A,s} \tag{3}$$

$$C_{m,b} = \frac{\cot\phi}{6}\left[\left(1 - 2\tan^2\phi\right)\left(1 - \psi^3\cos^3\phi\right) - 3\left(1 - \psi\cos\phi\right)\psi^2\cos^2\phi\right]C_{N,c,\phi} + \frac{\psi^2}{2}\left[\left(1 - \psi\cos\phi\right)\cot\phi - \psi\sin\phi\right]C_{N,s} \tag{4}$$

The normal-force and axial-force coefficients of the base flares referenced to A_b are

$$C_{N,f} = \left[\left(\frac{r_f}{r_b}\right)^2 - 1\right]C_{N,c,\theta} \tag{5}$$

and

$$C_{A,f} = \left[\left(\frac{r_f}{r_b}\right)^2 - 1\right]C_{A,c,\theta} \tag{6}$$

respectively. If the body is considered to be composed of separate components, then the force coefficient equations for the complete configurations may be written as follows:

$$C_N = \left(1 - \psi^2\cos^2\phi\right)C_{N,c,\phi} + \psi^2 C_{N,s} + C_{N,f} \tag{7}$$

$$C_A = \left(1 - \psi^2\cos^2\phi\right)C_{A,c,\phi} + \psi^2 C_{A,s} + C_{A,f} \tag{8}$$

The axial distance $\bar{x}$ between the center of pressure of the base flare and the cone-flare juncture is

$$\bar{x} = \frac{\left(r_f - r_b\right)\left(r_b + 2r_f\right)}{3\left(r_b + r_f\right)}\cot\theta \tag{9}$$

Thus, it follows from equations (4) and (9) that the pitching-moment-coefficient equation for the complete configuration may be written as

$$C_{m,b} = \frac{\cot \phi}{6}\left[\left(1 - 2\tan^2\phi\right)\left(1 - \psi^3\cos^3\phi\right) - 3(1 - \psi\cos\phi)\psi^2\cos^2\phi\right]C_{N,c,\phi} + \frac{\psi^2}{2}\left[(1 - \psi\cos\phi)\cot\phi - \psi\sin\phi\right]C_{N,s} - C_{N,f}\left(\frac{\bar{x}}{2r_b}\right) \quad (10)$$

The pitching-moment-coefficient equation about some reference point located on the axis of symmetry ahead of the cone-flare juncture may be expressed as

$$C_m = C_{m,b} - C_N\left(\frac{x}{2r_b}\right) \quad (11)$$

where x is the distance between the cone-flare juncture and the moment reference point on the axis of symmetry.

In the preceding development, the effects of forebody shading on the base flare have been neglected. (See eqs. (7), (8), and (10).) If the shading had been considered, the effect would have been an increase in C_N, a decrease in C_A, and an increase in the stability.

RESULTS AND DISCUSSION

Schlieren and Oil Flow Studies

Schlieren photographs for $0^\circ \leq \alpha \leq 45^\circ$ are presented in figure 2. Oil flow photographs for $\alpha = 0^\circ$ are presented in figure 3. A summary plot, obtained from figures 2 and 3, showing the extent of separation as a function of bluntness ratio for constant flare angles is presented in figure 4. A comparison of the transition Reynolds numbers presented in references 11 and 12 for 10° cones with the local Reynolds numbers for the present investigation indicates that the separation was laminar. It is of interest to note that the flow separated further forward for $\psi = 0.255$ than for $\psi = 0$ for both the 30° and 60° flares. (See fig. 4.) This indicates that for a constant flare angle the separation point moves forward to some maximum as the bluntness ratio increases from zero and then moves rearward with further increases in bluntness ratio. The initial increase in the extent of separation with small bluntness ratios is probably due to the reduction of local Mach number. However, experimental results for bluntness ratios in the range $0 < \psi < 0.255$ would be required to establish the location of this maximum. The decrease in separation with increasing bluntness ratio beyond $\psi = 0.255$ is attributed to the decrease in local Reynolds number since the local Mach number remains esentially constant with increasing ψ. (See ref. 13.) Oil flow photographs of models II-30F and II-60F for $\alpha = 40^\circ$ are presented in figure 5. These together with figure 2 clearly indicate the

complex flow field at angles of attack greater than zero due to flow separation, viscous cross flow, and shock interaction.

Experimental Force and Moment Characteristics

The effects of bluntness ratio on the static aerodynamic characteristics of the unflared cones are presented in figure 6. These data were previously presented in figure 5 of reference 3 and are included in the present paper for comparison purposes. All pitching-moment coefficients are presented about an arbitrary point on the axis of symmetry located $0.2r_b$ ahead of the centroid of the cone planform area. These points are labeled Moment reference center in figure 1. Equations for readily obtaining the location of the centroid of the planform area for spherically blunted cones are presented in the appendix of reference 3. (Note that the pitching-moment-coefficient data in reference 3 are presented about the base of the cones.)

The effects of increasing flare angle on the aerodynamic characteristics for a constant bluntness ratio are presented in figures 7 and 8. Boundary-layer separation (see refs. 14 and 15) and the dynamic-pressure distribution between the model surface and the bow shock wave (see ref. 16) may have a large influence on the effectiveness of conical base flares.

Boundary-layer separation effects on the aerodynamic characteristics of flare-stabilized bodies are usually manifested by a reduction in C_A, an increase in the positive slope of C_N, and an increase in stability near zero angle of attack. (See refs. 14 and 15.) Boundary-layer separation on the windward side of the model usually decreases or disappears as α increases. Consequently, the force and moment coefficient curves usually become coincident or nearly parallel with those curves resulting for configurations having no separation over the entire angle-of-attack range.

The dynamic-pressure distribution in the flow field between the model surface and the bow shock wave at the cone-flare juncture may also have an important effect on flare effectiveness. (See ref. 16.) In reference 16 it was shown for nose-cylinder-flare bodies that a region of nearly constant low dynamic pressure existed adjacent to the model surface. This region was joined to an outer region of nearly linearly increasing dynamic pressure by an intermediate region in which the gradients were very large. Increasing nose bluntness was shown to increase the extent of the low dynamic-pressure region near the model surface, but had little if any effect on the distribution near the shock wave. The position of the flare relative to the region in which the dynamic pressure changed rapidly was shown to affect the effectiveness of the flare.

In a conical flow field the extent of the low, nearly constant dynamic-pressure region adjacent to the body would be negligible in comparison with that presented in reference 16 for a cylindrical flow field. Consequently, the flares in the present investigation,

neglecting viscosity, would extend into the high dynamic-pressure region at all angles of attack and flare effectiveness would not be strongly influenced by the strong dynamic-pressure gradients. Bluntness, however, would have the tendency to increase the extent of the low dynamic pressure near the body and therefore could have a strong influence on flare effectiveness at all angles of attack.

In the present investigation extensive separation existed at zero angle of attack, and the reattachment points could not be accurately defined. Therefore it was not possible to obtain a meaningful inviscid flow-field calculation in which the separation region would be replaced by a constant pressure surface. As a consequence, the interplay of the dynamic-pressure distribution and separation and their effects on the effectiveness of the flares could not be separated in the present analysis.

The value of C_A at $\alpha = 0^o$ for model I-60F was only slightly greater than that of model I-30F. (See fig. 7.) This difference is attributed to the decrease in C_A with increasing separation (refs. 14 and 15) and to the difference in flare surface areas. (Note that the surface area of the 30^o flare was $\sqrt{3}$ times that of the 60^o flare and that both sets of data were reduced by using the same reference area πr_b^2.) The effect of separation appears to vanish as α increases to 5^o. As previously mentioned, $\left(C_{N_\alpha}\right)_{\alpha=0}$ increases with increasing separation (refs 14 and 15). Consequently, the increase in $\left(C_{N_\alpha}\right)_{\alpha=0}$ due to separation decreases with increasing ψ. (See fig. 7.) The stability parameter $\left(C_{m_\alpha}\right)_{\alpha=0}$ for the flared configurations decreases with increasing ψ. This decrease is probably due to the reduction in separation with increasing bluntness ratio. The stability also decreases with increasing α near $\alpha = 0^o$ for models I-30F, I-60F, II-30F, and II-60F (see figs. 7(a) and 7(b)); however, it increases for models III-30F, III-60F, IV-30F, and IV-60F (see figs. 7(c) and 7(d)). This reversal in the trend of stability with increasing α is probably due to the combined effects of the dynamic-pressure distribution and separation on the flare effectiveness, since, as previously mentioned, the dynamic-pressure effects would be expected to increase with increasing ψ and α, whereas the extent of separation would be expected to decrease. The marked decrease in the stability with increasing angle of attack (see fig. 7) is attributed to a decrease in the pressure acting on the flare due to the expansion wave reflected at the intersection of the bow shock wave and the flare shock wave (ref. 17). Reference 17 shows that a considerable decrease or complete loss of longitudinal stability may occur for angles of attack which cause the intersection between the bow shock wave and the flare shock wave to be in the vicinity of the flare surface. It should be noted that the expansion fan originating at the intersection of the separation and reattachment shocks may also affect the stability characteristics of the flare and, furthermore, the expansion fan may affect the stability at a much lower angle of attack than that for the bow-shock—flare-shock intersection.

Furthermore, a compression wave may originate at this intersection depending upon the Mach number and flow-field geometry behind the bow shock wave. (See ref. 18.)

The curves of L/D as a function of α for the sharp cone models are similar in that, for a given value of α, L/D decreases with increasing flare angle. (See fig. 8(a).) However, this trend is not present for the blunt cone models. For example, model II-30F has a higher value of L/D than either model II or II-60F for $0^{\circ} < \alpha < 6.5^{\circ}$. (See fig. 8(b).) The angle-of-attack range over which this trend occurs increases with increasing ψ to a value of $0^{\circ} < \alpha < 33.5^{\circ}$ for $\psi = 0.763$. (See figs. 8(b) to 8(d).) These trends are attributed to the combined effects of separation and dynamic-pressure distribution. However, it should also be noted that Newtonian impact theory predicts that the L/D contribution of the 30° flare is positive throughout the entire angle-of-attack range of the present investigation whereas that of the 60° flare is negative. (See table V(f) of ref. 10.)

Lift-drag polars are presented in figure 9. The adverse pressure gradients produced by the flares caused the flow to separate well ahead of the cone-flare juncture at $\alpha = 0$. (See fig. 4.) This separation resulted in a loss in effectiveness of the flare as an aerodynamic drag device. For example, models I and I-30F had drag coefficients at zero lift of approximately 0.105 and 0.345, respectively, which represents an approximate increase in drag of 330 percent. However, model I-60F had a value of 0.385 for an increase in drag of 336 percent in comparison to model I. This indicates that little if any gain in aerodynamic drag would result in a flare angle of 60° as compared with an angle of 30°. As previously mentioned, the flare base diameter was held constant during the present investigation. Consequently, these results may be altered somewhat for a workable extensible base-flare drag device where the base diameter increases with increasing θ while the surface area remains constant.

The effects of bluntness ratio for a given base flare on the force and moment coefficients are presented in figures 10 and 11. The experimental data appear to separate into two distinct groups near $\alpha = 0^{\circ}$; that is, near $\alpha = 0^{\circ}$ models I-30F and II-30F have similar characteristics with increasing α and models III-30F and IV-30F have similar characteristics. (See figs. 10(a) and 11(a).) This grouping is also present for the 60° flares. (See figs. 10(b) and 11(b).) The separation of the experimental force and moment coefficients into these two distinct groups near $\alpha = 0^{\circ}$ is probably due to the reduction in the extent of separated flow with increasing ψ. (See fig. 4.) It is also of interest to note the crossover in C_A at $\alpha = 0^{\circ}$ for models I-30F and II-30F (see fig. 10(a)) and for models I-60F and II-60F (see fig. 10(b)). This crossover cannot be attributed wholly to separation, but is thought to be the result of the combined separation and dynamic-pressure distribution effects.

Comparison of Experimental and Theoretical Results

Comparisons between experimental force and moment coefficients and Newtonian impact theory approximations of these values are presented in figure 12. As was previously shown in reference 3, Newtonian impact theory accurately predicts the trends and, in many instances, the actual magnitudes of the force and moment coefficients within the experimental accuracy of the data for the unflared cones. However, the agreement between theory and experimental data is poor for the flared models. This poor agreement can be attributed to a combination of laminar separation, viscous crossflow, bow-shock position relative to the model surface, and shock interaction in the vicinity of the flare. An interesting point is the agreement between theoretical and experimental pitching-moment coefficients for models III-30F and IV-30F for angles of attack up to 5° and 10°, respectively. (See figs. 12(c) and 12(d).) The stability at zero lift is well predicted for both models. The improvement with increasing ψ is probably due to a combination of the decrease in separation (see fig. 4) and the position of the shock interaction point in relation to the flare surface; that is, for a given angle of attack, the shock interaction point moves further from the flare surface with increasing ψ. (See fig. 2 and ref. 8.) The agreement between Newtonian theory and experimental data would be expected to improve for smaller flare angles than those tested during the present experimental program since the flare-induced separation would decrease. (See the trend established in fig. 4.)

CONCLUSIONS

An experimental investigation to determine the aerodynamic characteristics of a series of 10° semiapex-angle spherically blunted cones with 30° and 60° semiapex-angle base flares has been completed. The tests were made in the Langley 11-inch hypersonic tunnel at a Mach number of 9.75 and a Reynolds number based on cone base diameter of 1.56×10^5 for angles of attack from 0° to 45°. Analysis of the results of the investigation has yielded the following conclusions:

1. The configurations were statically stable about a point on the axis of symmetry located one-tenth of a cone base diameter ahead of the centroid of the cone planform area.

2. Flare-induced flow separation decreased with increasing bluntness ratio for a given flare angle and increased with increasing flare angle for a constant bluntness ratio.

3. In general, agreement was poor between experimental force and moment coefficients for the flared cones and Newtonian impact theory estimates of these values.

Langley Research Center,
National Aeronautics and Space Administration,
Langley Station, Hampton, Va., June 16, 1966.

REFERENCES

1. Allen, H. Julian; Seiff, Alvin; and Winovich, Warren: Aerodynamic Heating of Conical Entry Vehicles at Speeds in Excess of Earth Parabolic Speed. NASA TR R-185, 1963.

2. Demele, Fred A.: A Study of the Convective and Radiative Heating of Shapes Entering the Atmospheres of Venus and Mars at Superorbital Speeds. NASA TN D-2064, 1963.

3. Harris, Julius E.: Force-Coefficient and Moment-Coefficient Correlations and Air-Helium Simulation for Spherically Blunted Cones. NASA TN D-2184, 1964.

4. Wilkinson, David B; and Harrington, Shelby A.: Hypersonic Force, Pressure, and Heat Transfer Investigations of Sharp and Blunt Slender Cones. AEDC-TDR-63-177, U.S. Air Force, 1963.

5. Edenfield, E. E.: Comparison of Hotshot Tunnel Force, Pressure, Heat-Transfer and Shock Shape Data With Shock Tunnel Data. AEDC-TDR-64-1, U.S. Air Force, Jan. 1964.

6. Schippell, Herbert R.; Neal, Luther, Jr.; and Marcum, Don C., Jr.: Aerodynamic Characteristics of Two Trailblazer II Blunted 9^{o} Cone Reentry Bodies at Mach 6.8 in Air and 21.2 in Helium. NASA TN D-2786, 1965.

7. Champney, W. B.; Athans, J. B.; and Mayerson, C. D.: A Study of Hypersonic Aerodynamic Drag Devices. WADC Tech. Rept. 59-324, Pt. II, U.S. Air Force, June 1961.

8. McLellan, Charles H.; Williams, Thomas W.; and Bertram, Mitchel H.: Investigation of a Two-Step Nozzle in the Langley 11-Inch Hypersonic Tunnel. NACA TN 2171, 1950.

9. Stine, Howard A.; and Wanlass, Kent: Theoretical and Experimental Investigation of Aerodynamic-Heating and Isothermal Heat-Transfer Parameters on a Hemispherical Nose With Laminar Boundary Layer at Supersonic Mach Numbers. NACA TN 3344, 1954.

10. Wells, William R.; and Armstrong, William O.: Tables of Aerodynamic Coefficients Obtained From Developed Newtonian Expressions for Complete and Partial Conic and Spheric Bodies at Combined Angles of Attack and Sideslip With Some Comparisons With Hypersonic Experimental Data. NASA TR R-127, 1962.

11. Nagamatsu, H. T.; and Sheer, R. E., Jr.: Boundary-Layer Transition on a 10^{o} Cone in Hypersonic Flows. AIAA J., vol. 3, no. 11, Nov. 1965, pp. 2054-2061.

12. Potter, J. Leith; and Whitfield, Jack D.: Boundary-Layer Transition Under Hypersonic Conditions. Recent Developments in Boundary Layer Research, Pt. III, AGARDograph 97, May 1965, pp. 1-62.

13. Miller, D. S.; Hijman, R.; and Childs, M. E.: Mach 8 to 22 Studies of Flow Separations Due to Deflected Control Surfaces. Presented at the AIAA Summer Meeting, Los Angeles, California, June 17-20, Paper No. 63-173, 1963. AIAA J., vol. 2, no. 2, Feb. 1964, pp. 312-321.

14. Dennis, David H.: The Effects of Boundary-Layer Separation Over Bodies of Revolution With Conical Tail Flares. NACA RM A57I30, 1957.

15. Gray, J. Don: Boundary Layer Separation Effects on the Static Stability of a Flared-Tail Missile Configuration at M = 2 to 5. AEDC-TN-60-103, U.S. Air Force, 1960.

16. Ashby, George C., Jr.; and Cary, Aubrey M., Jr.: A Parametric Study of the Aerodynamic Characteristics of Nose-Cylinder-Flare Bodies at a Mach Number of 6.0. NASA TN D-2854, 1965.

17. Fitzgerald, Paul E., Jr.: The Effect of Bow-Shock—Flare-Shock Interaction on the Static Longitudinal Stability of Flare-Stabilized Bodies at Hypersonic Speeds. NASA TM X-664, 1962.

18. Zumwalt, Glen W.; and Flynn, John J., Jr.: Wave Reflection From the Intersection of Oblique Shock Waves of the Same Family. AIAA J., vol. 1, no. 9, Sept. 1963, pp. 2149-2150.

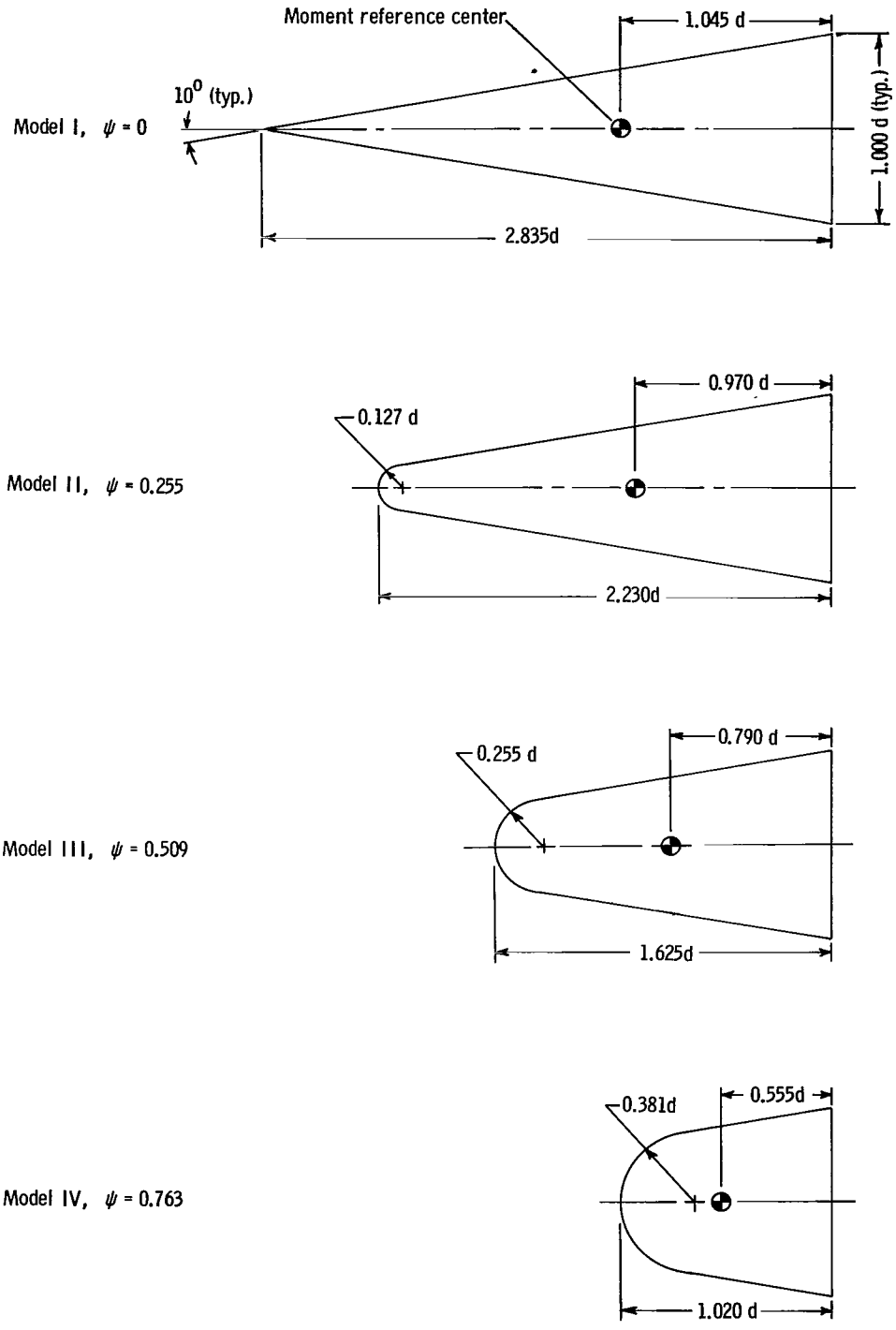

(a) Basic models. d = 1.5 in. (3.81 cm).

Figure 1.- Model drawings.

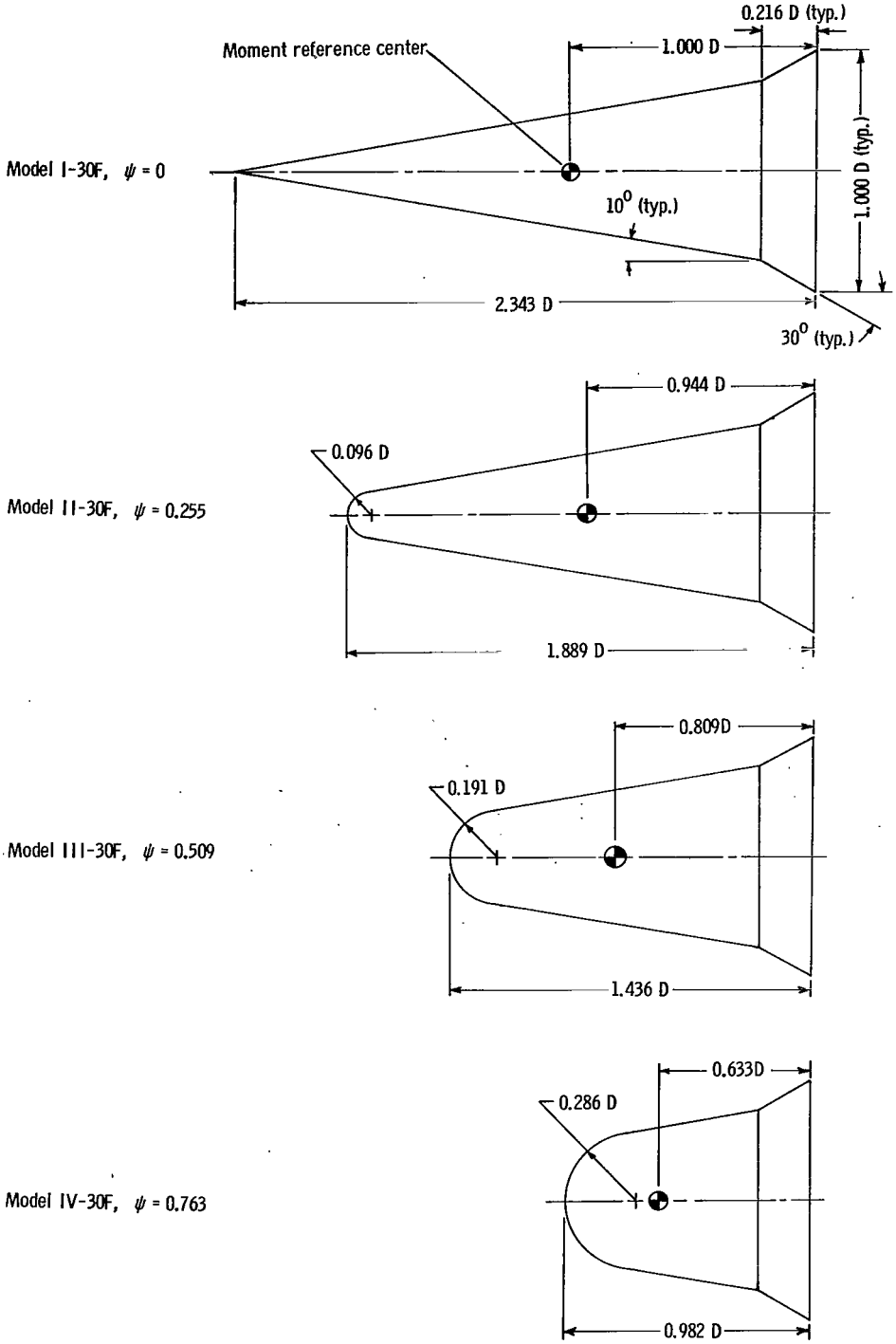

(b) 30^0 flare models. D = 2.00 in. (5.08 cm).

Figure 1.- Continued.

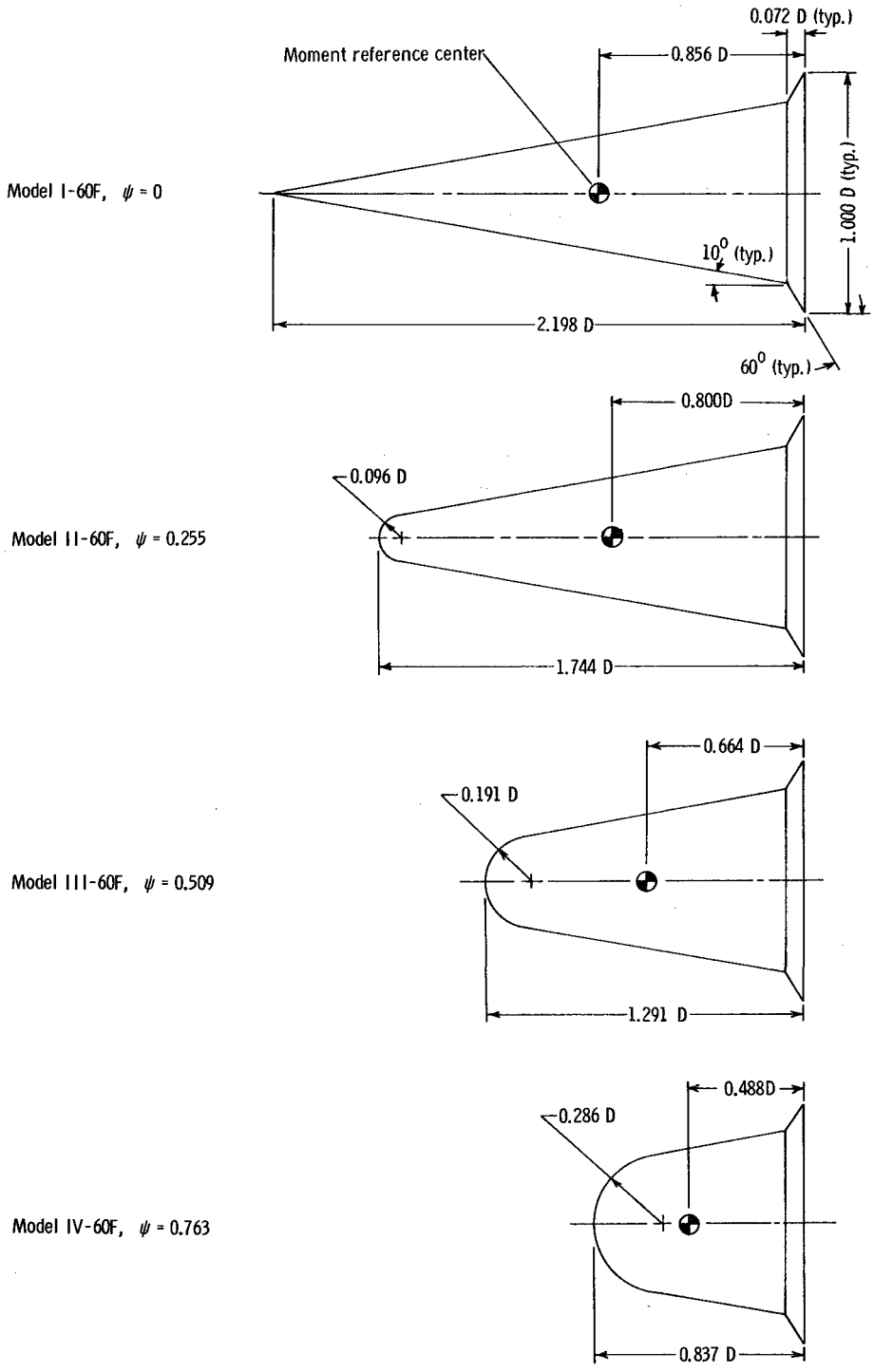

(c) 60° flare models. D = 2.00 in. (5.08 cm).

Figure 1.- Concluded.

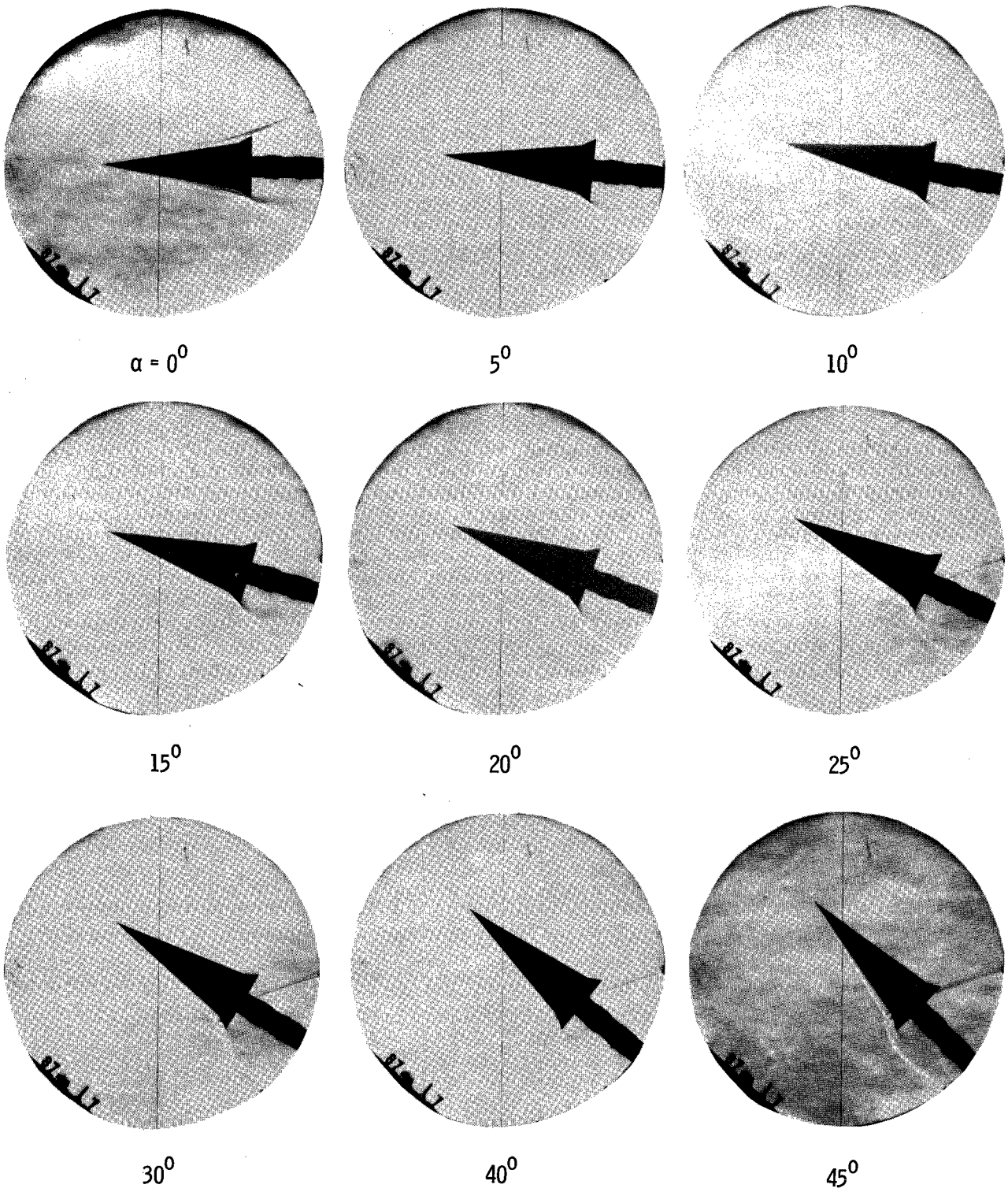

(a) Model I-30F; $\psi = 0$.

L-66-4458

Figure 2.- Schlieren photographs. $M_\infty = 9.75$; $R = 1.56 \times 10^5$.

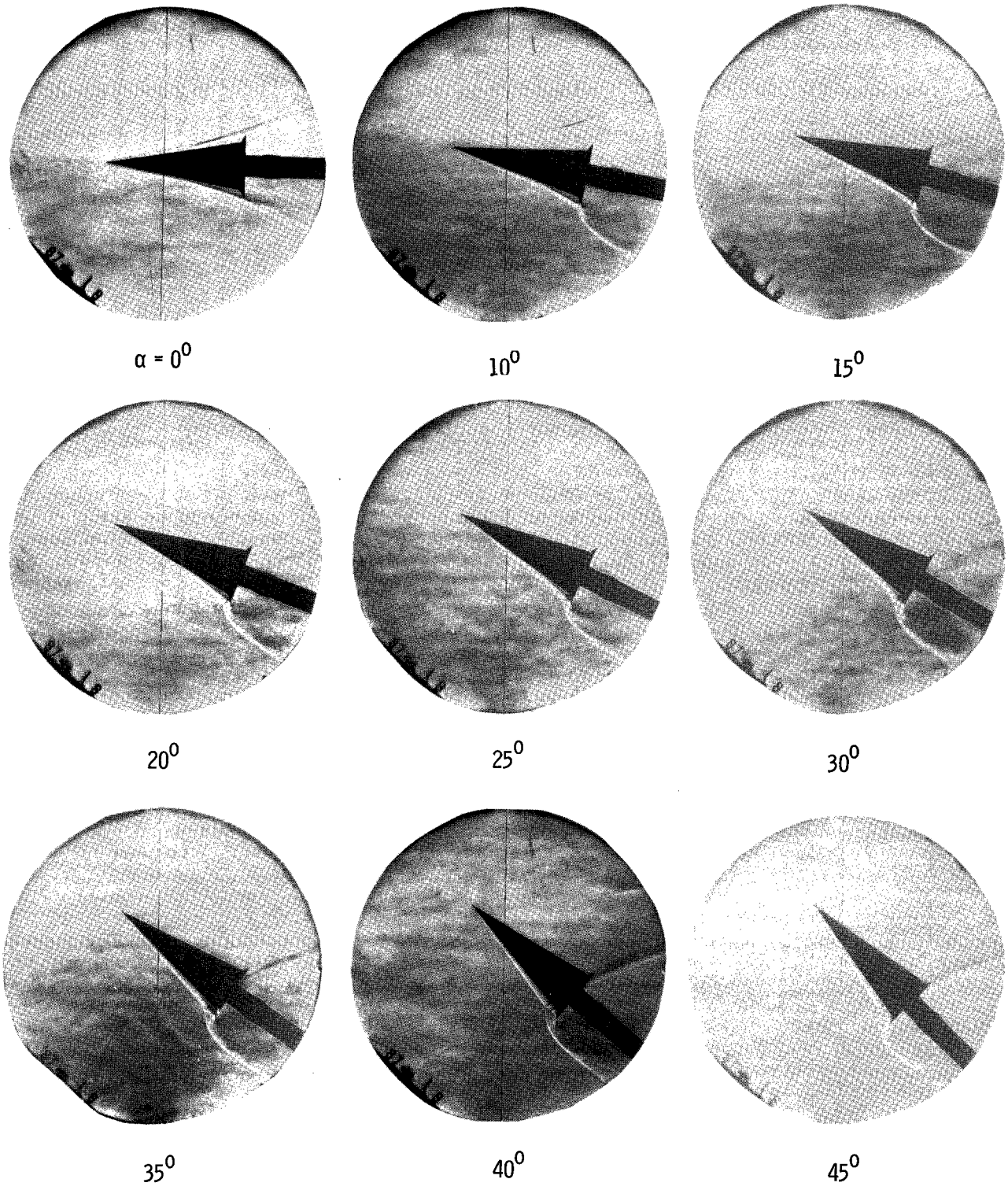

(b) Model I-60F; $\psi = 0$.

L-66-4459

Figure 2.- Continued.

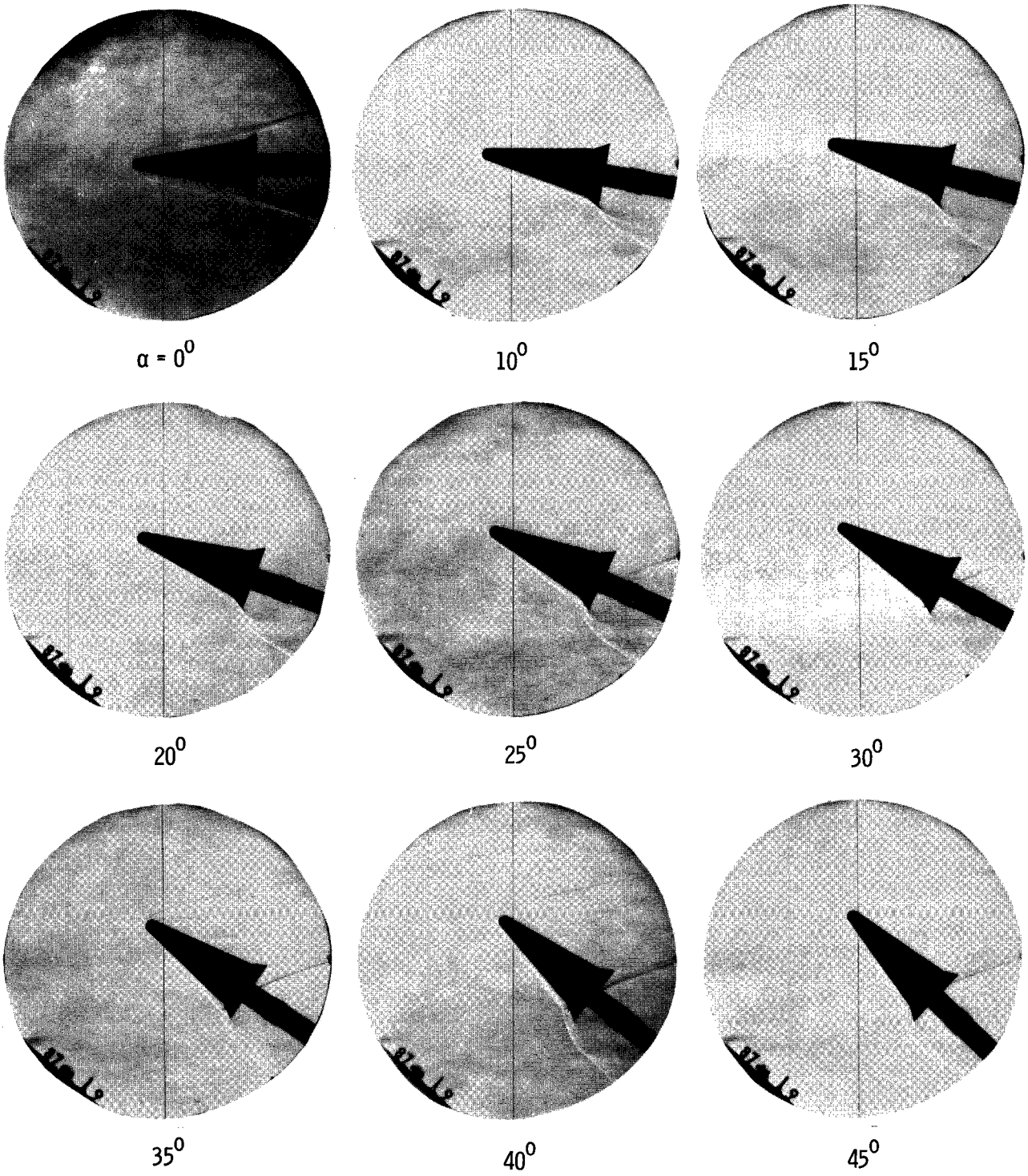

(c) Model 11-30F; ψ = 0.255.

L-66-4460

Figure 2.- Continued.

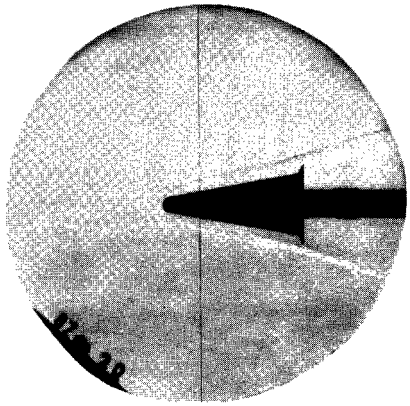

$\alpha = 0^0$

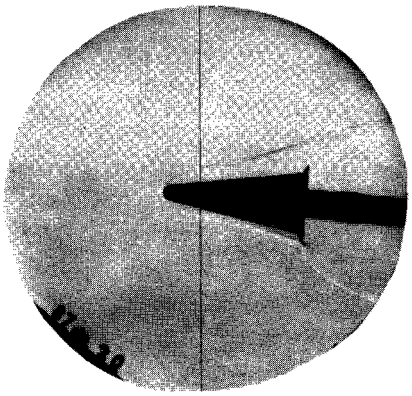

5^0

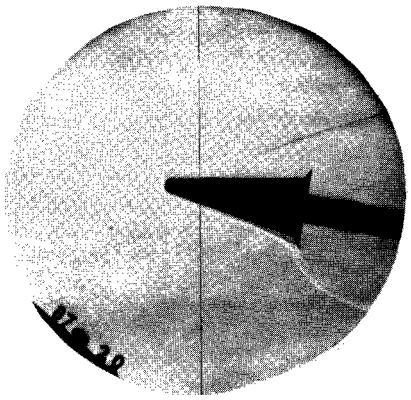

10^0

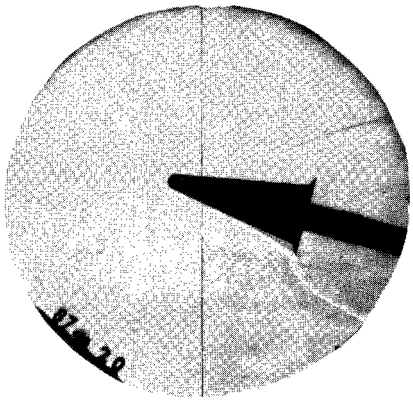

15^0

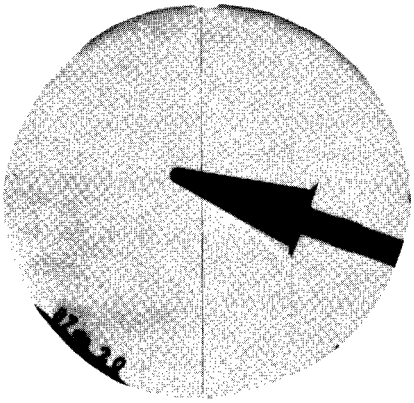

20^0

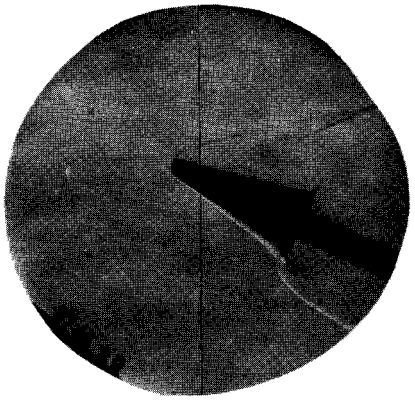

25^0

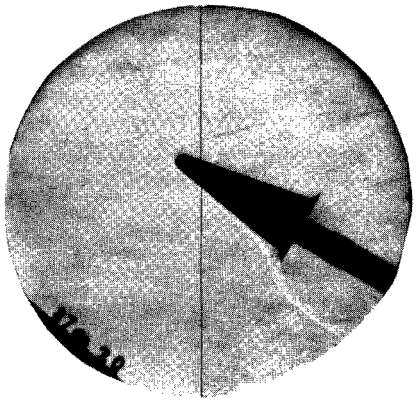

30^0

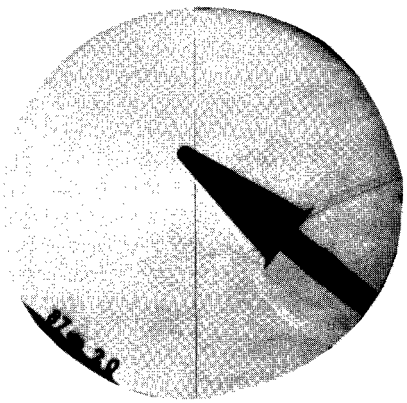

40^0

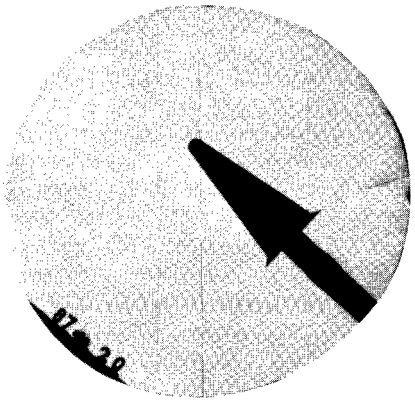

45^0

(d) Model 11-60F; $\psi = 0.255$.

L-66-4461

Figure 2.- Continued.

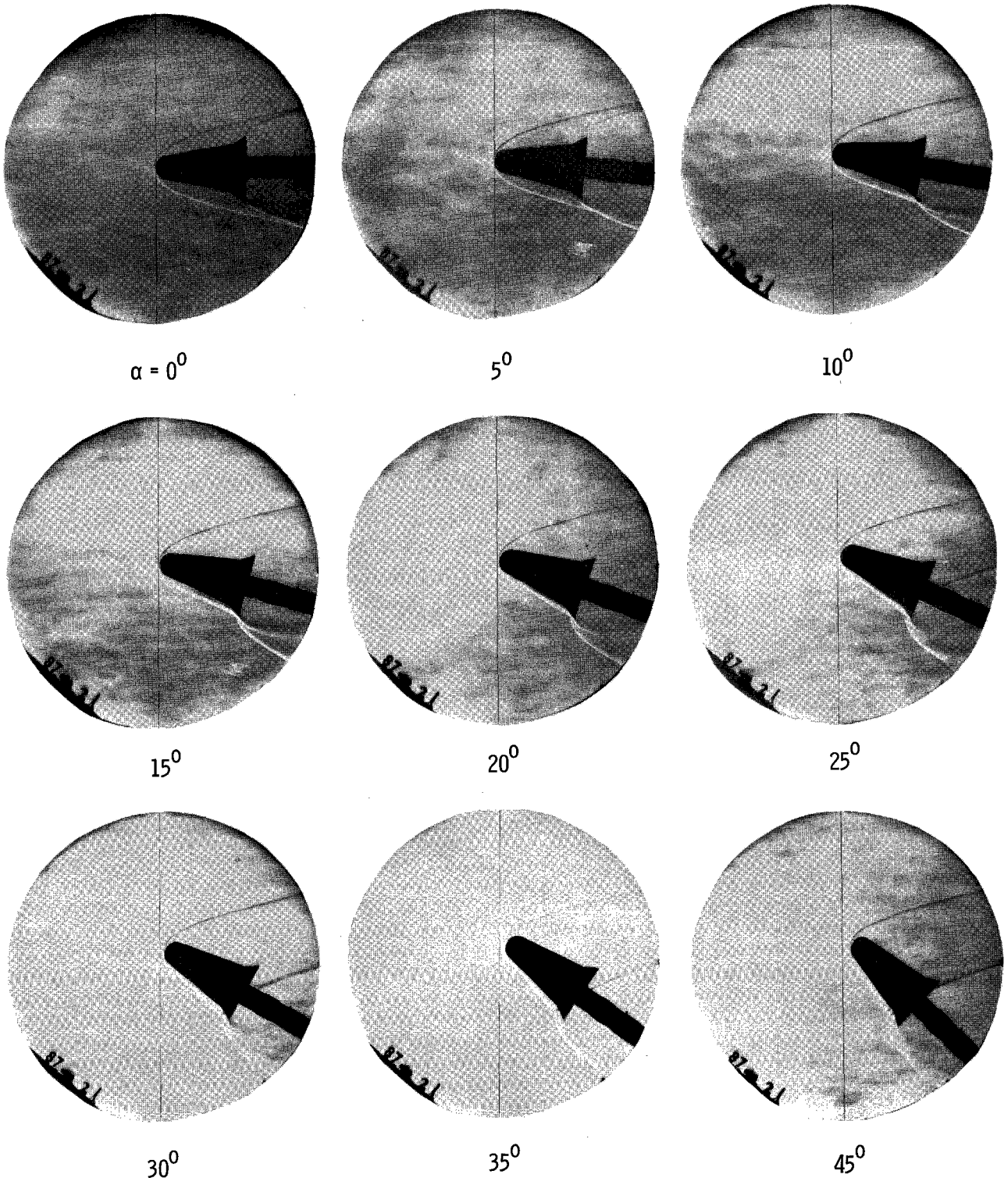

(e) Model 111-30F; ψ = 0.509. L-66-4462

Figure 2.- Continued.

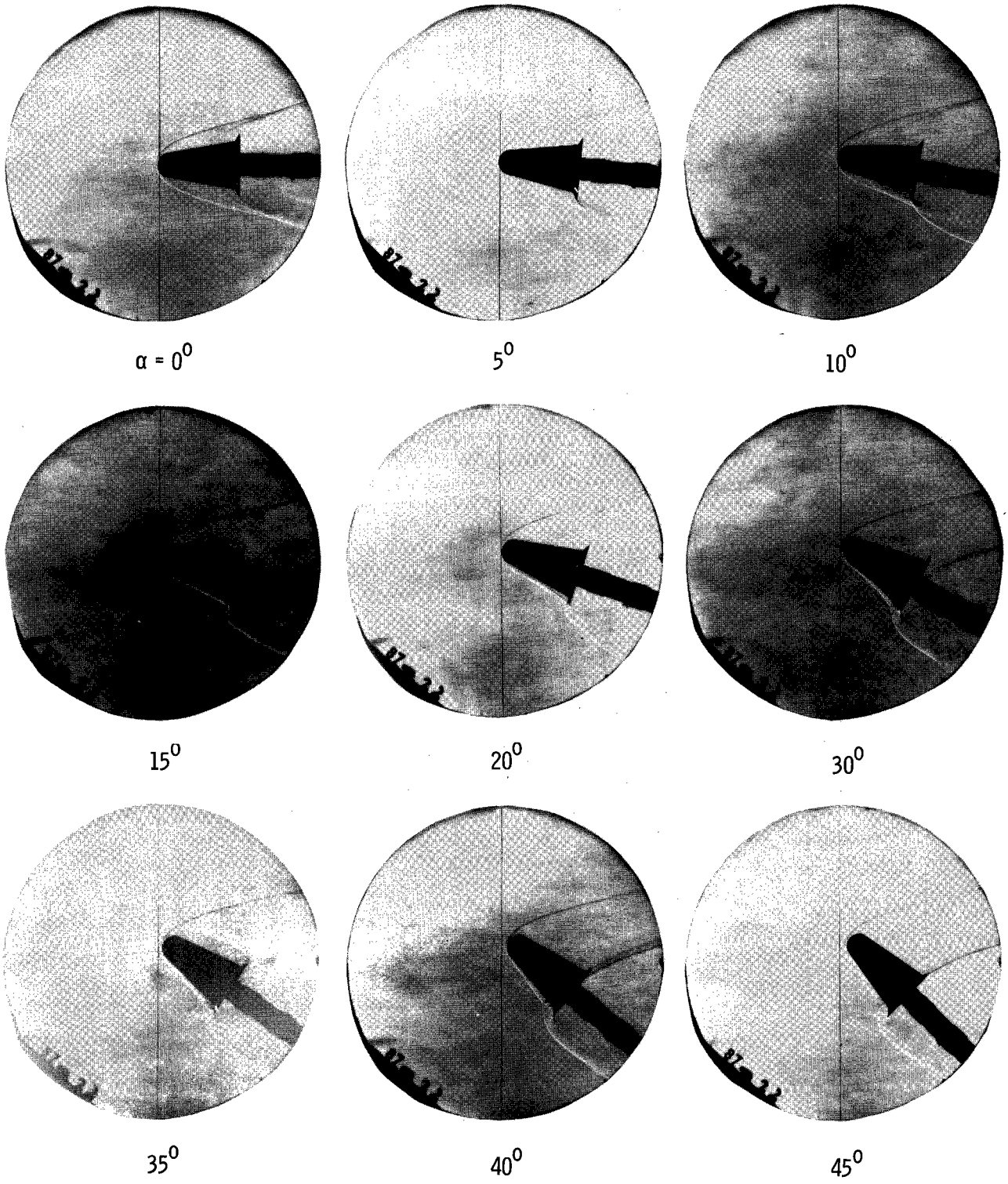

(f) Model III-60F; ψ = 0.509.

L-66-4463

Figure 2.- Continued.

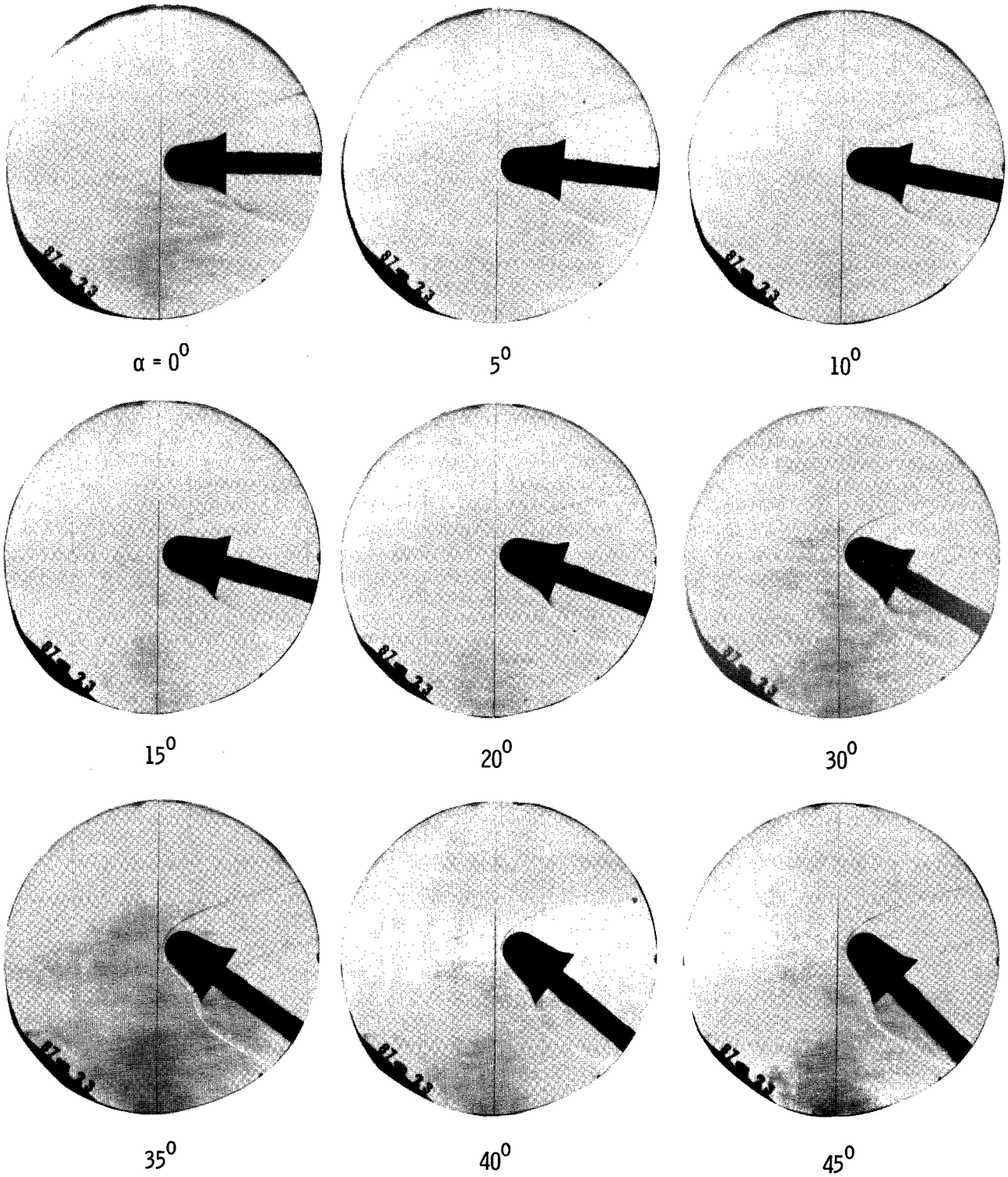

(g) Model IV-30F; ψ = 0.736.

L-66-4464

Figure 2.- Continued.

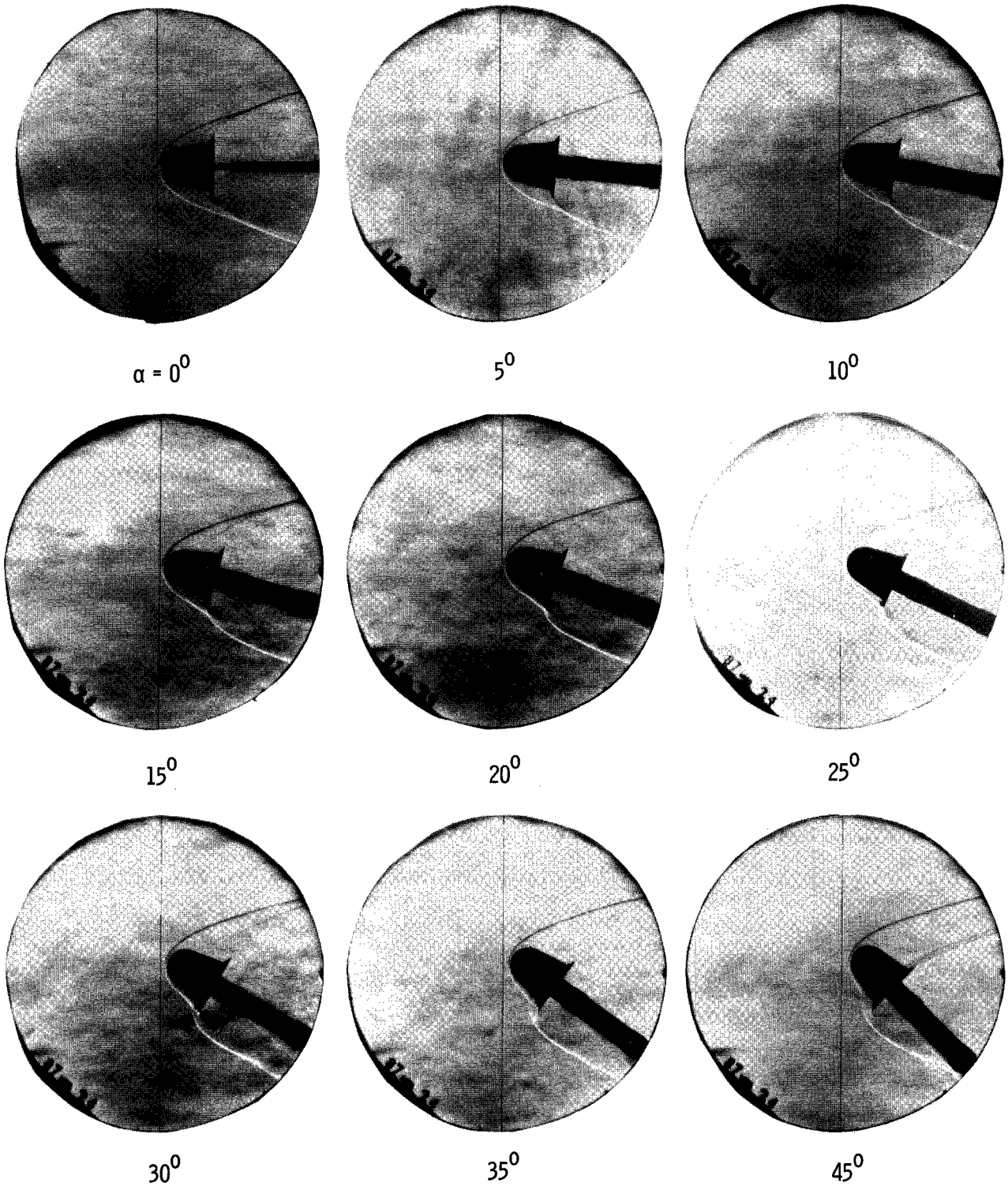

(h) Model IV-60F; $\psi = 0.763$. L-66-4465

Figure 2.- Concluded.

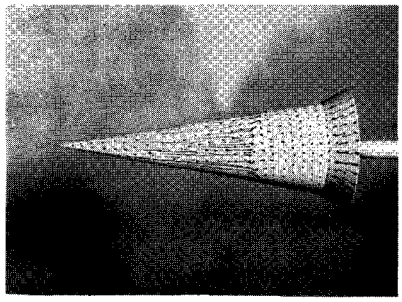

I-30 F

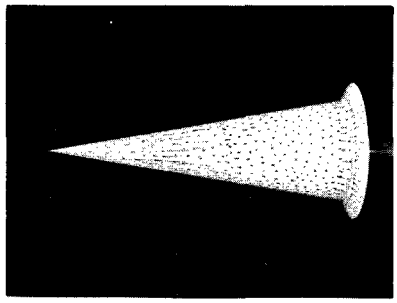

I-60 F

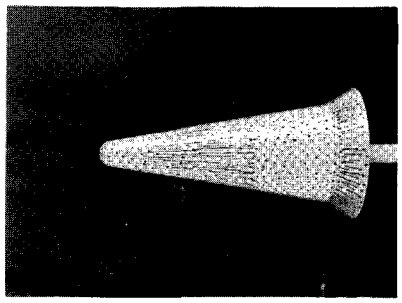

II-30 F

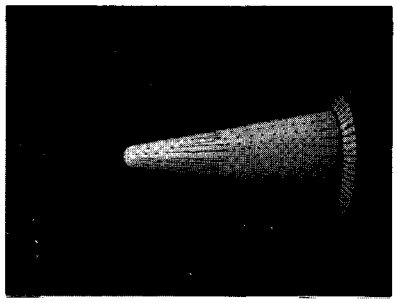

II-60 F

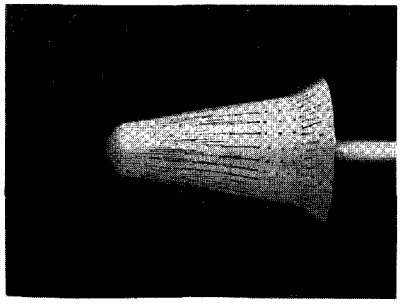

III-30 F

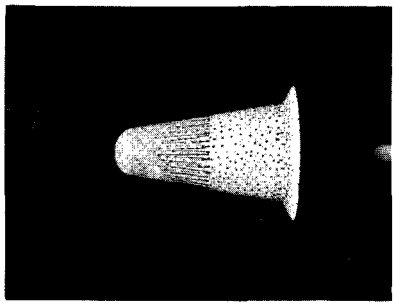

III-60 F

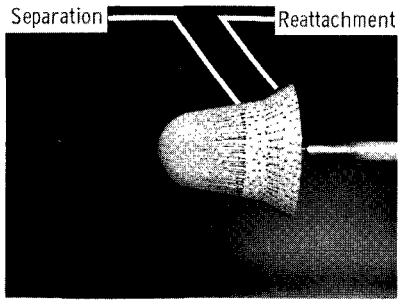

IV-30F

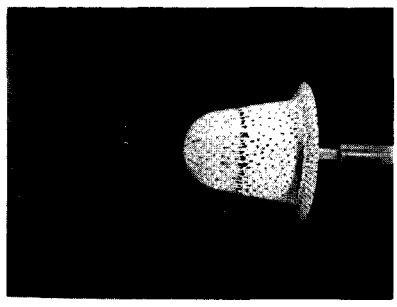

IV-60F

Figure 3.- Oil flow photographs. $M_\infty = 9.75$; $R = 1.56 \times 10^5$; $\alpha = 0^o$. L-66-4466

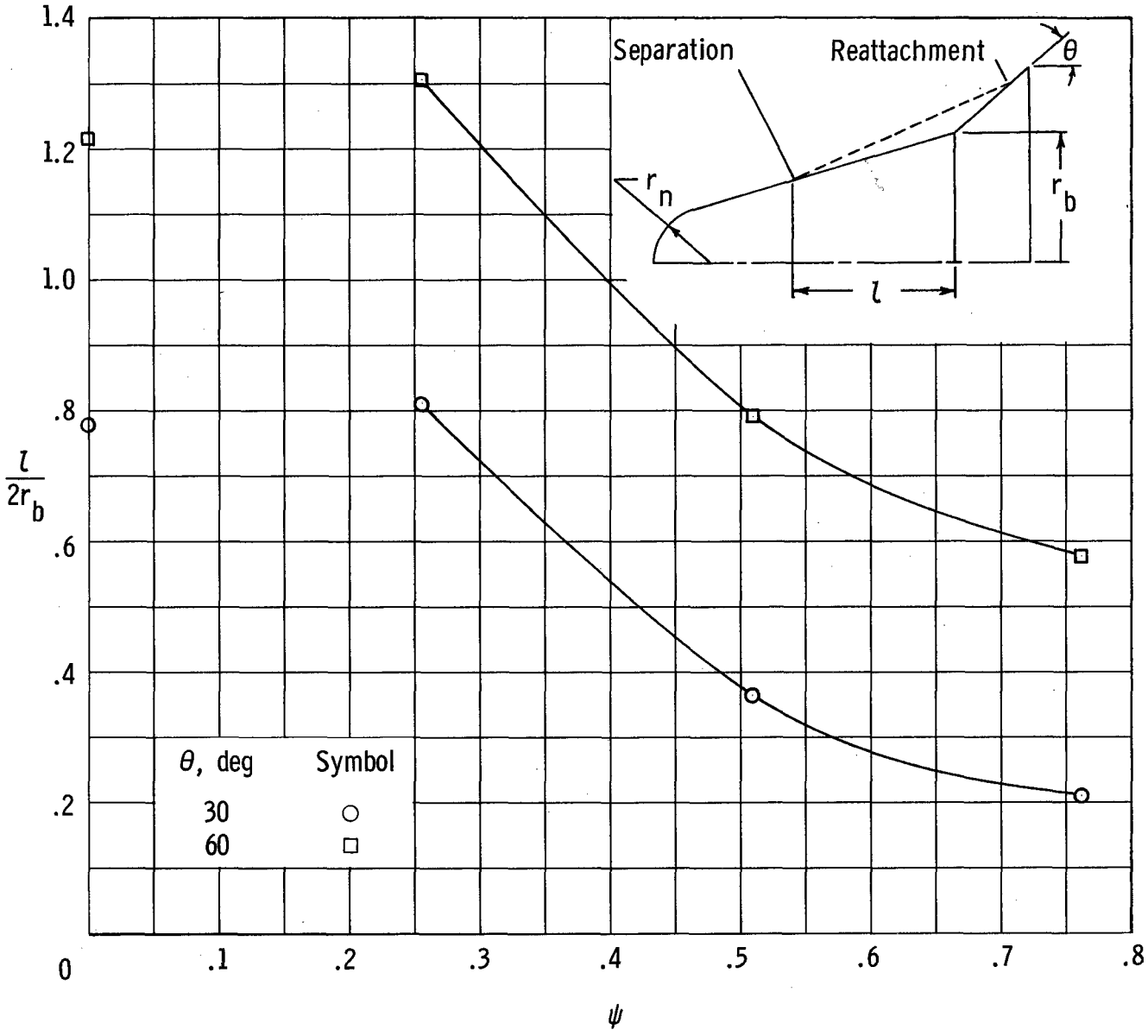

Figure 4.- Extent of separation. $M_\infty = 9.75$; $R = 1.56 \times 10^5$; $\alpha = 0^0$.

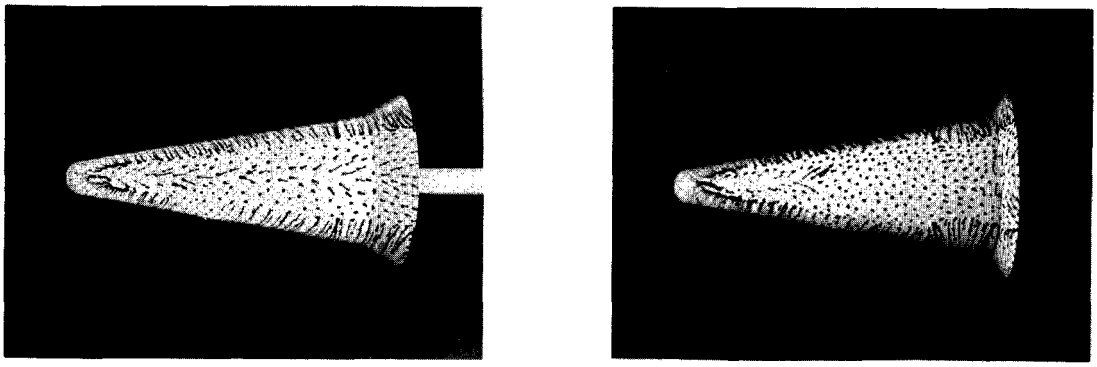

Leeward view

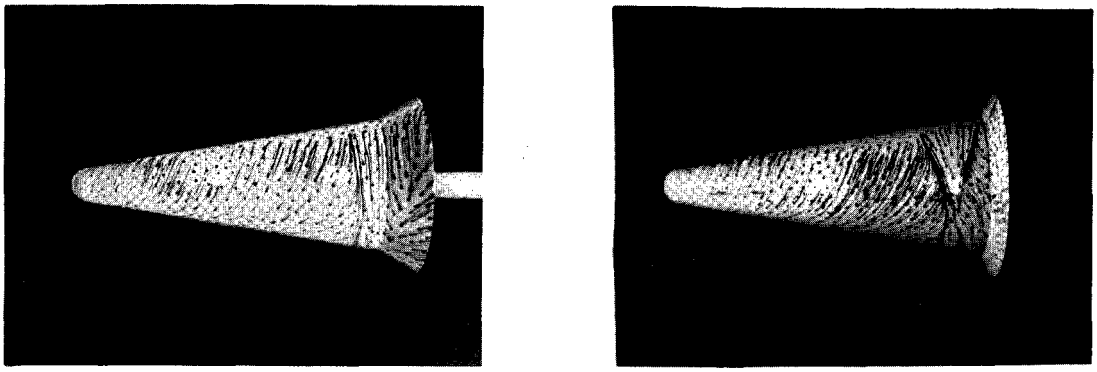

Side view

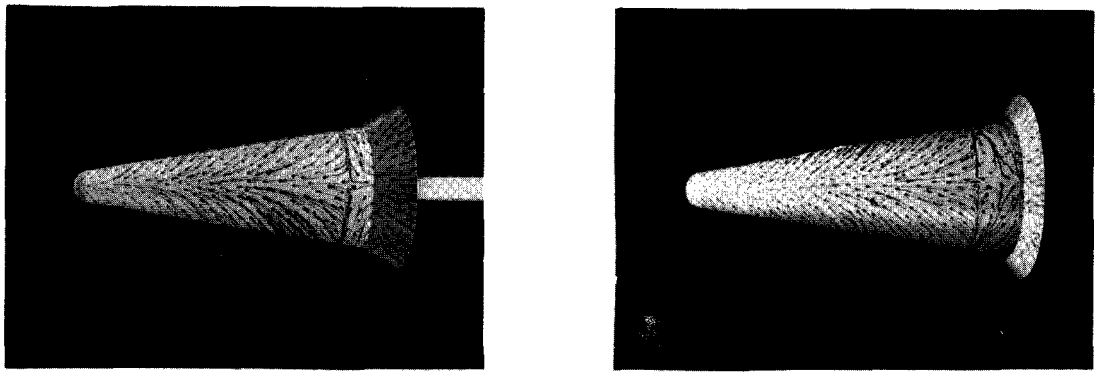

Windward view

Model 11-30F. Model 11-60F. L-66-4467

Figure 5.- Oil-flow photographs. $M_\infty = 9.75$; $R = 1.56 \times 10^5$; $\alpha = 40^\circ$.

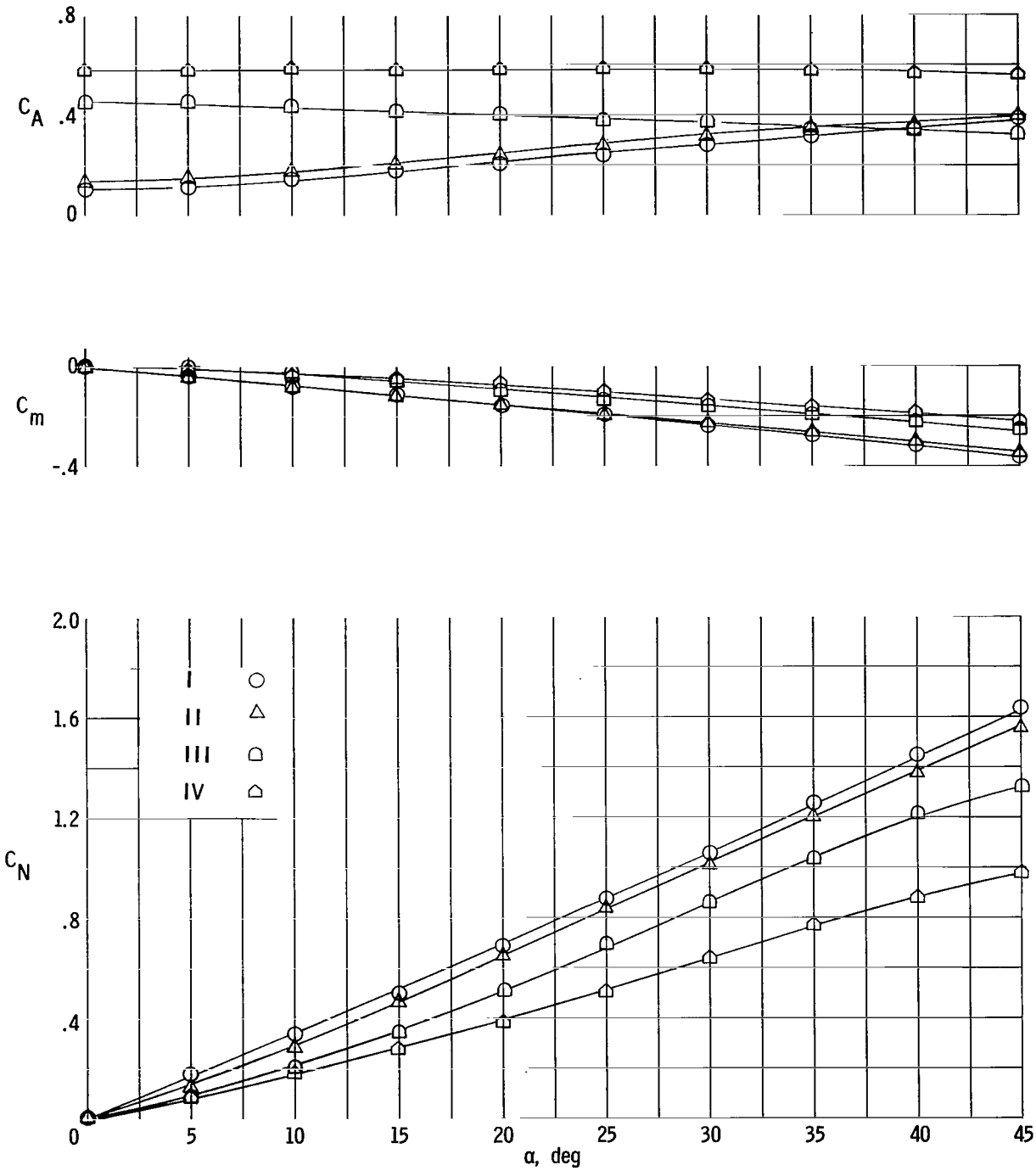

(a) Referred to body axis system.

Figure 6.- Effects of bluntness ratio on longitudinal force characteristics of a 10^0 semiapex-angle cone. $M_\infty = 9.75$; $R = 1.56 \times 10^5$.

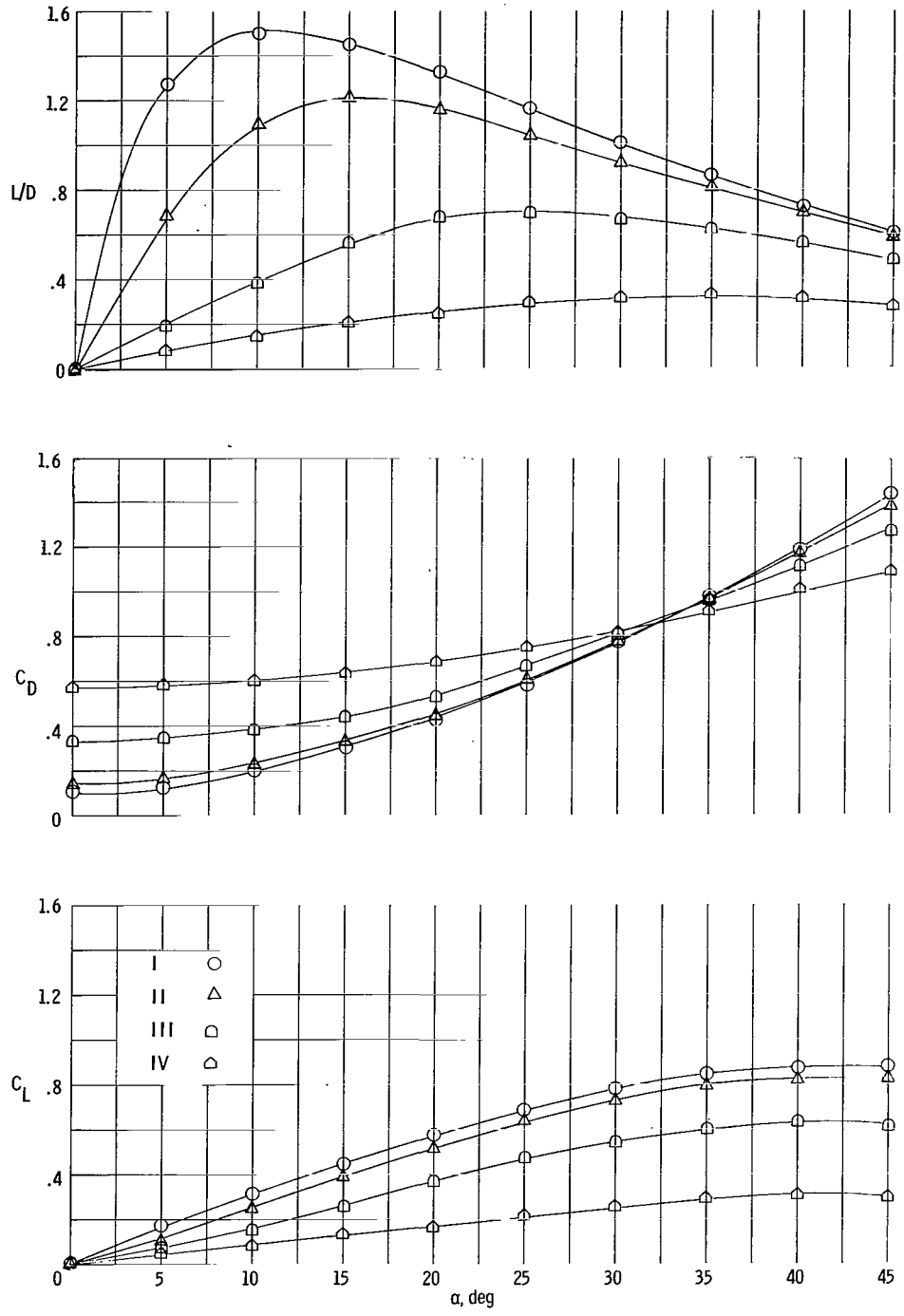

(b) Referred to stability axis system.

Figure 6.- Concluded.

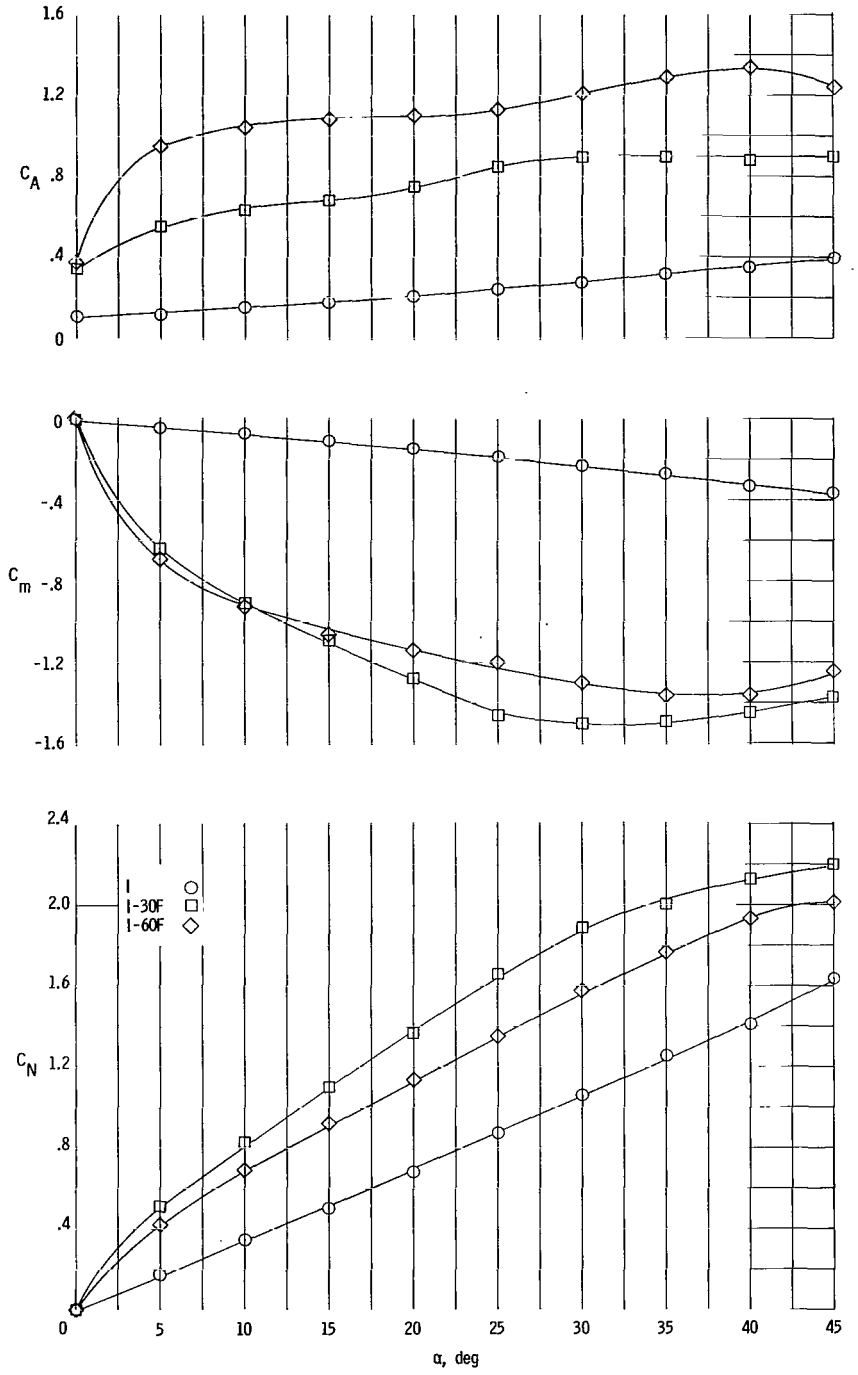

(a) $\psi = 0$.

Figure 7.- Effect of flare angle on longitudinal force characteristics of a 10^0 semiapex-angle cone referred to body axis system. $M_\infty = 9.75$; $R = 1.56 \times 10^5$.

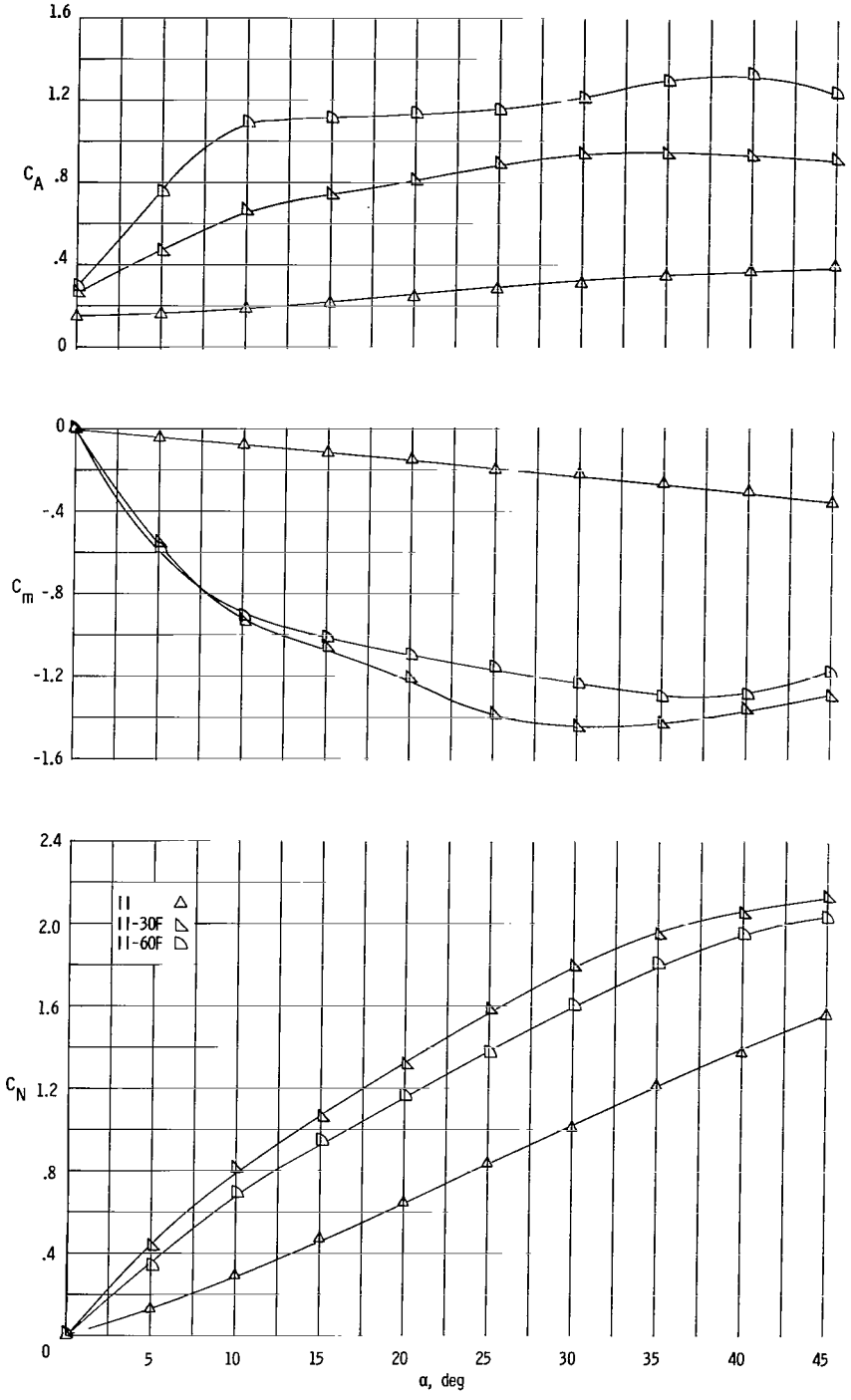

(b) $\psi = 0.255$.

Figure 7.- Continued.

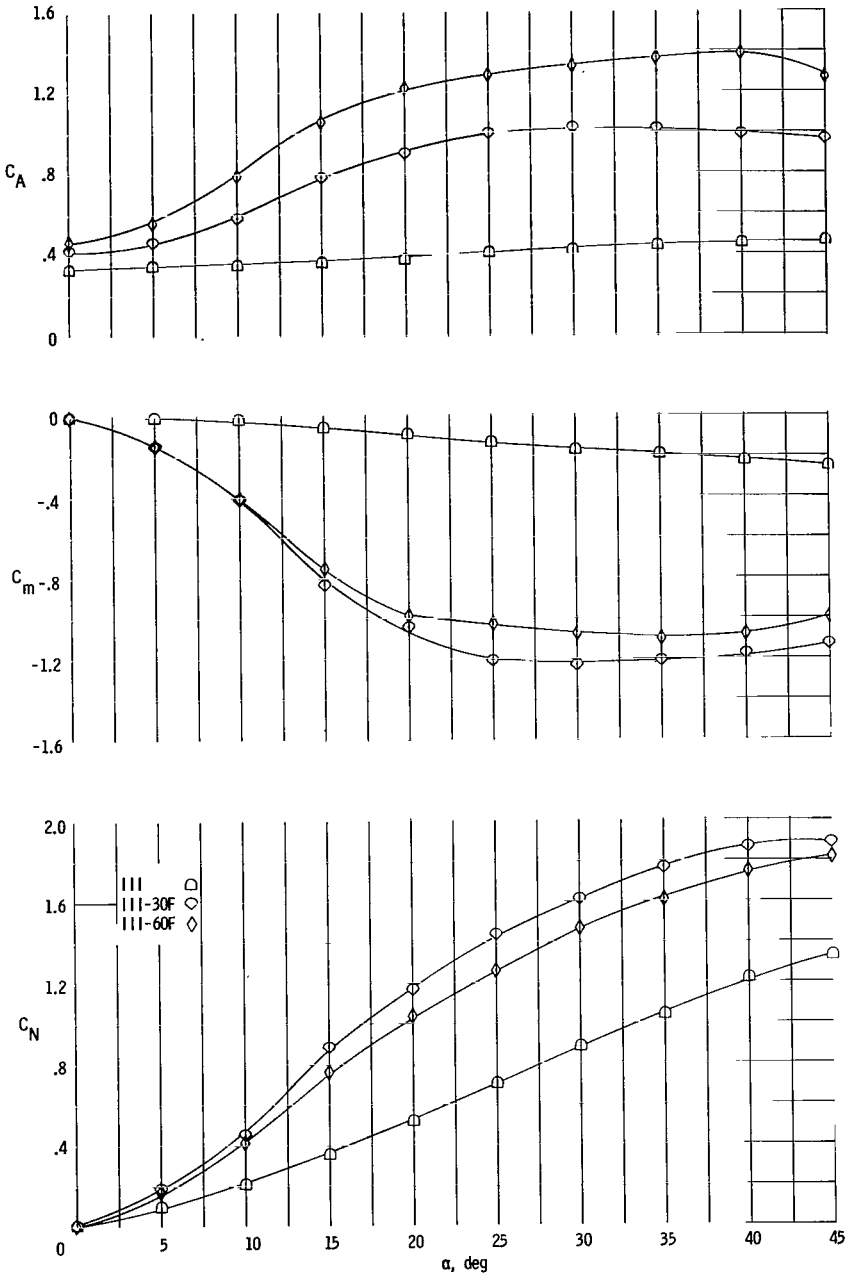

(c) $\psi = 0.509$.

Figure 7.- Continued.

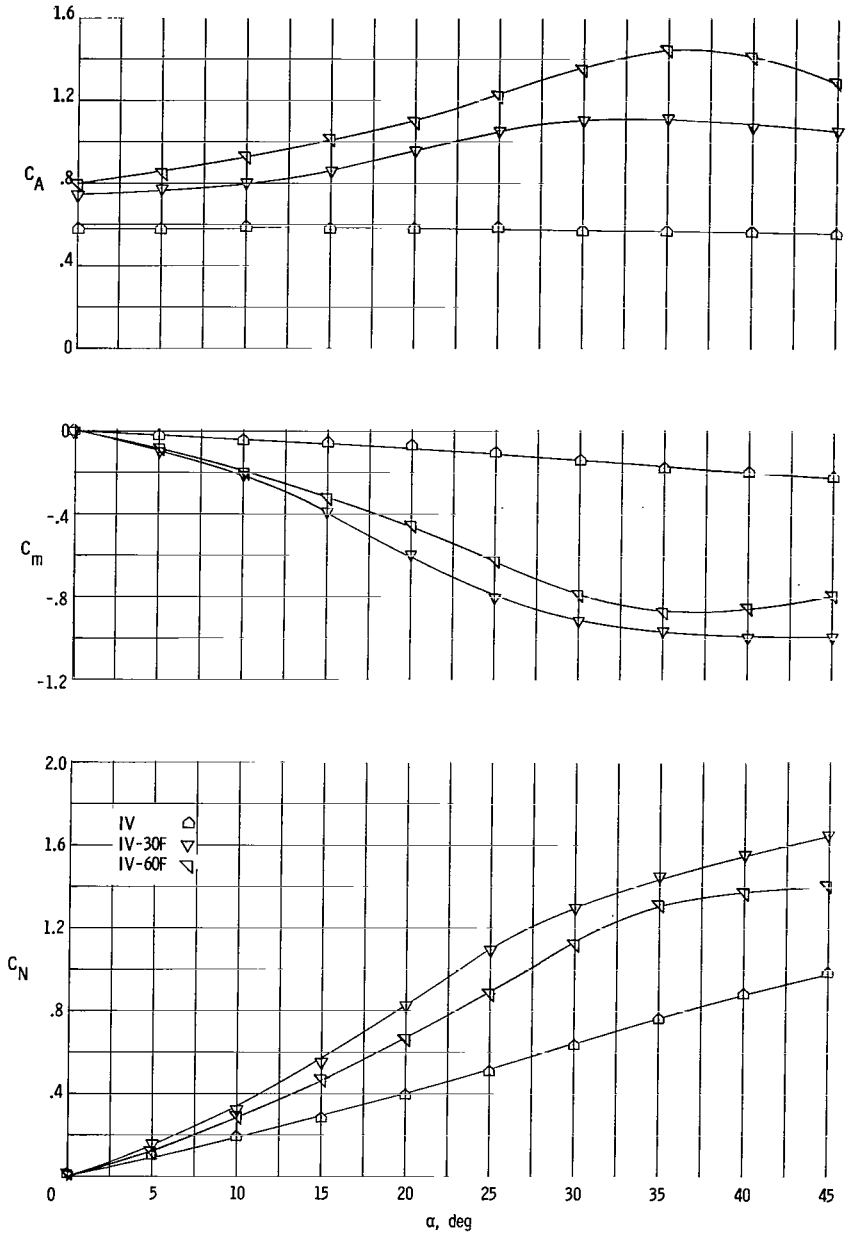

(d) $\psi = 0.763$.

Figure 7.- Concluded.

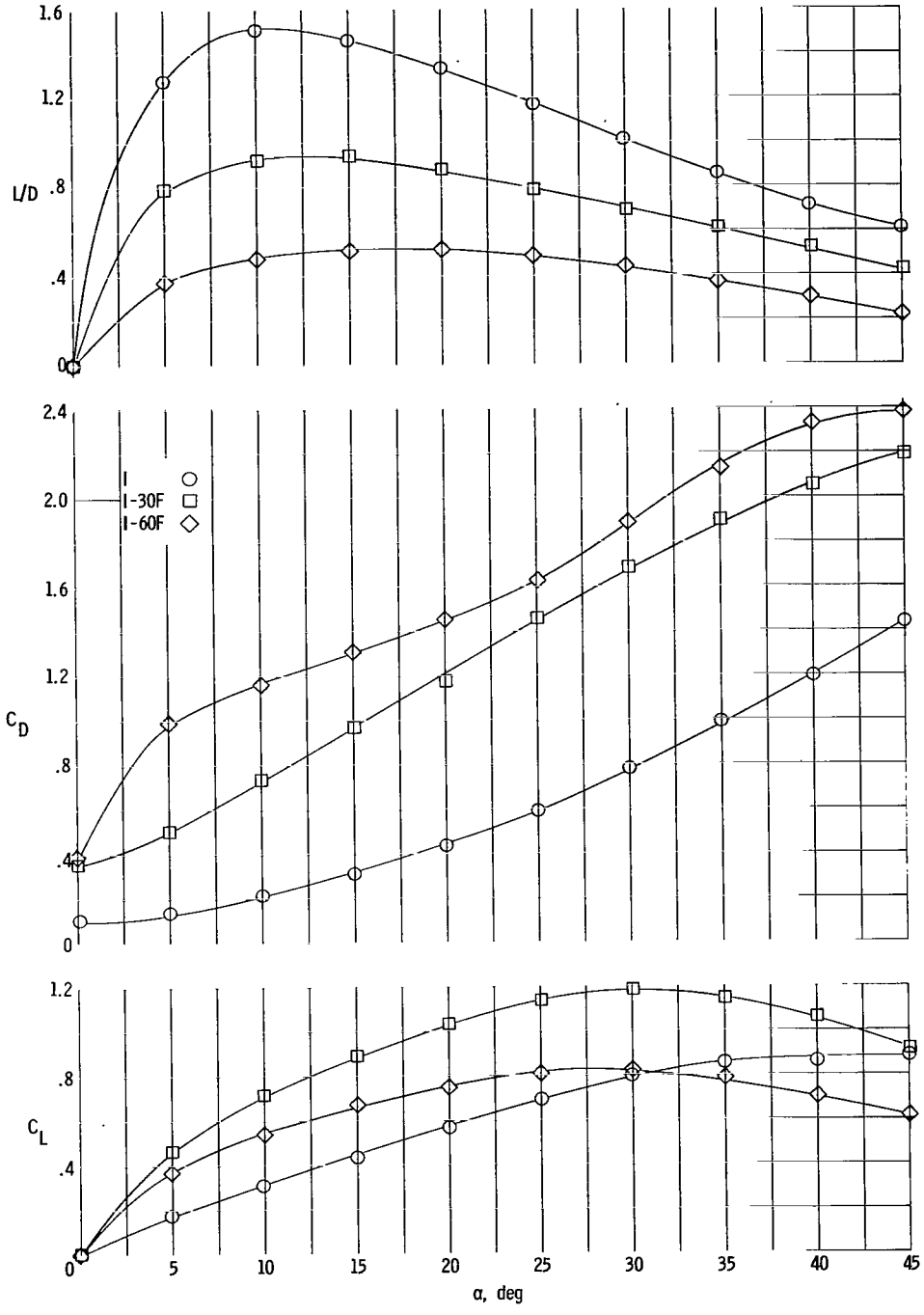

(a) $\psi = 0$.

Figure 8.- Effect of flare angle on longitudinal force characteristics of a 10^0 semiapex-angle cone referred to stability axis system. $M_\infty = 9.75$; $R = 1.56 \times 10^5$.

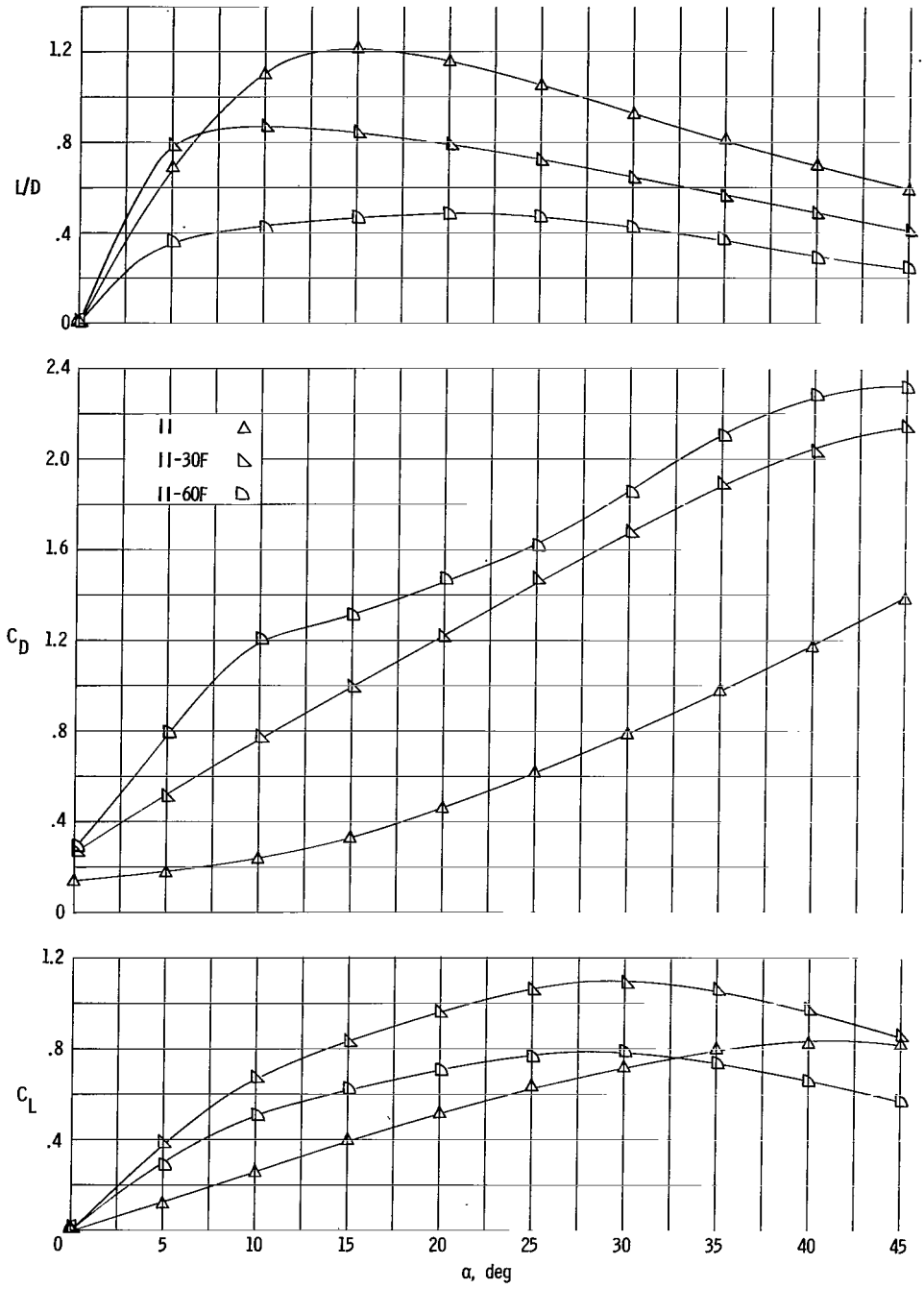

(b) $\psi = 0.255$.

Figure 8.- Continued.

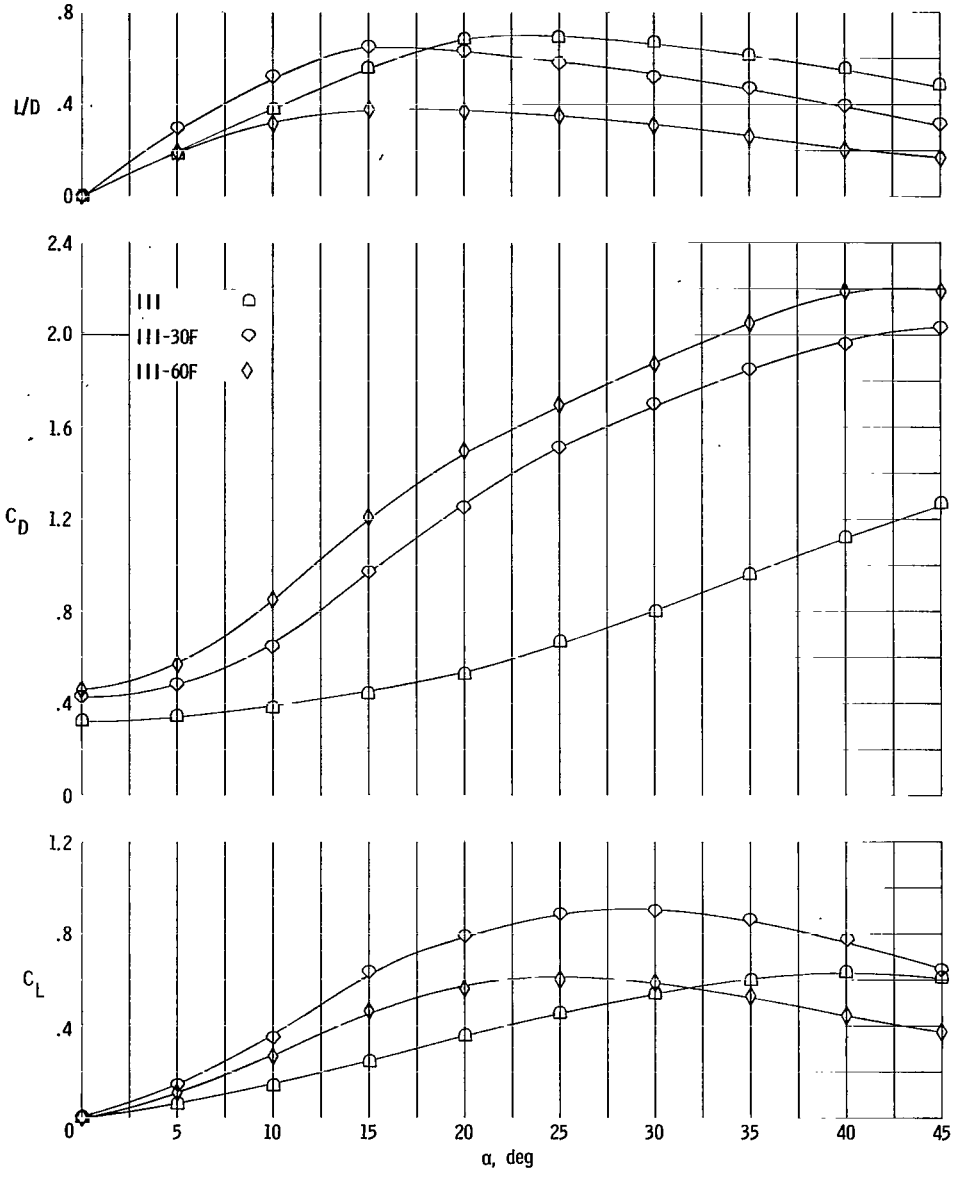

(c) $\psi = 0.509$.

Figure 8.- Continued.

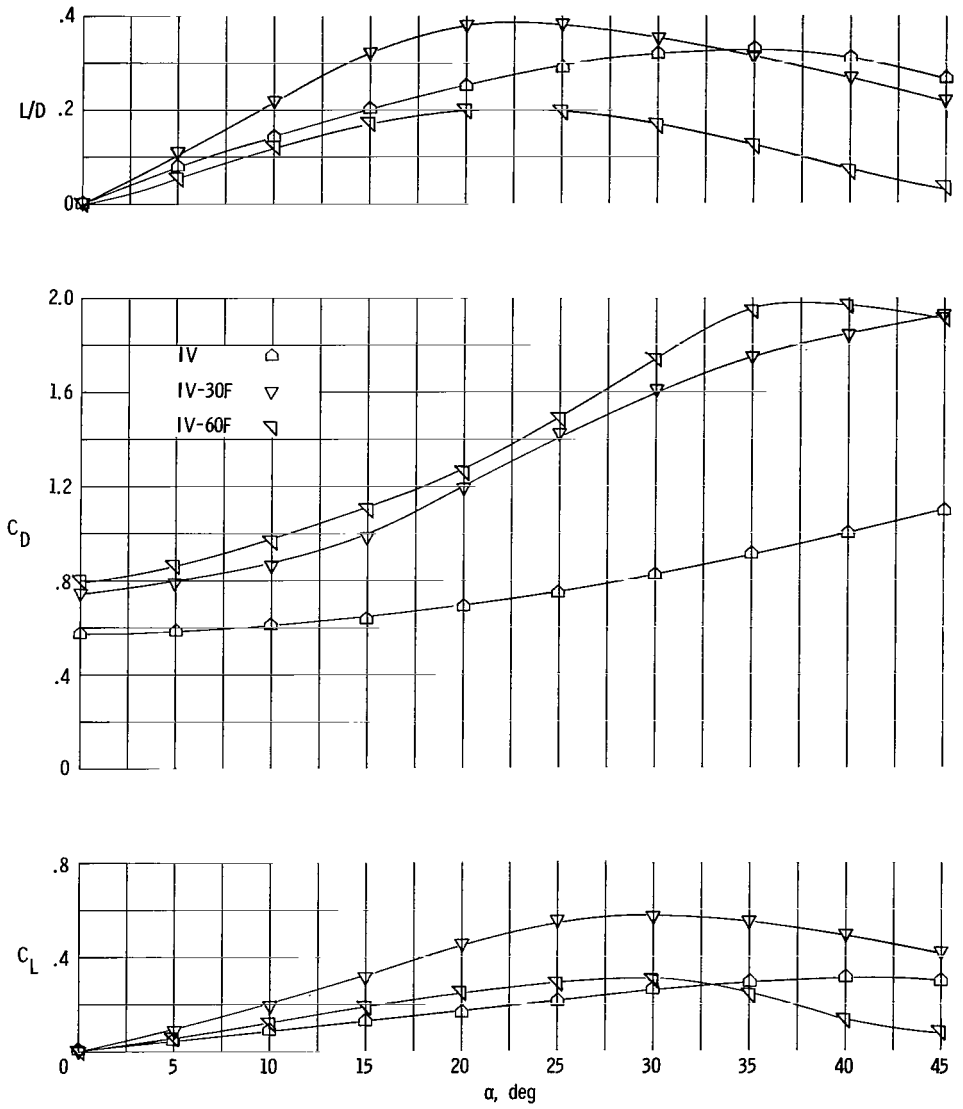

(d) $\psi = 0.763$.

Figure 8.- Concluded.

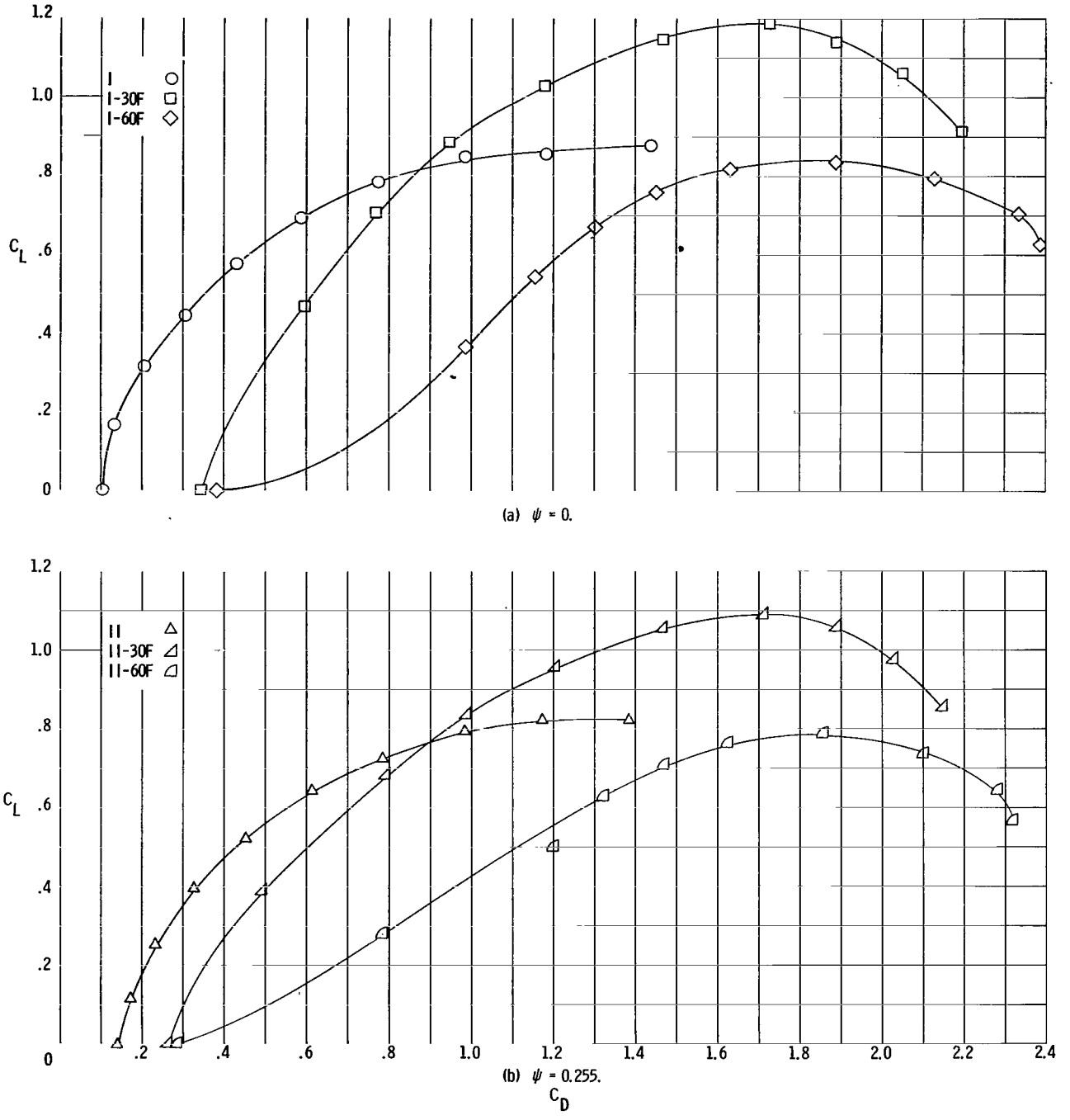

(a) $\psi = 0$.

(b) $\psi = 0.255$.

Figure 9.- Effect of flare angle on lift-drag polars. $M_\infty = 9.75$; $R = 1.56 \times 10^5$.

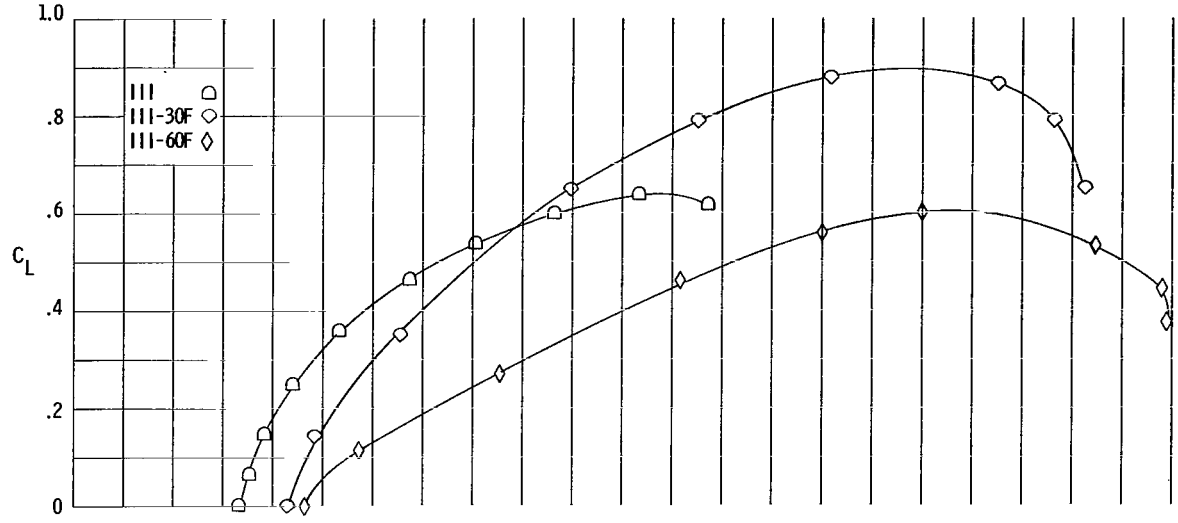

(c) ψ = 0.509.

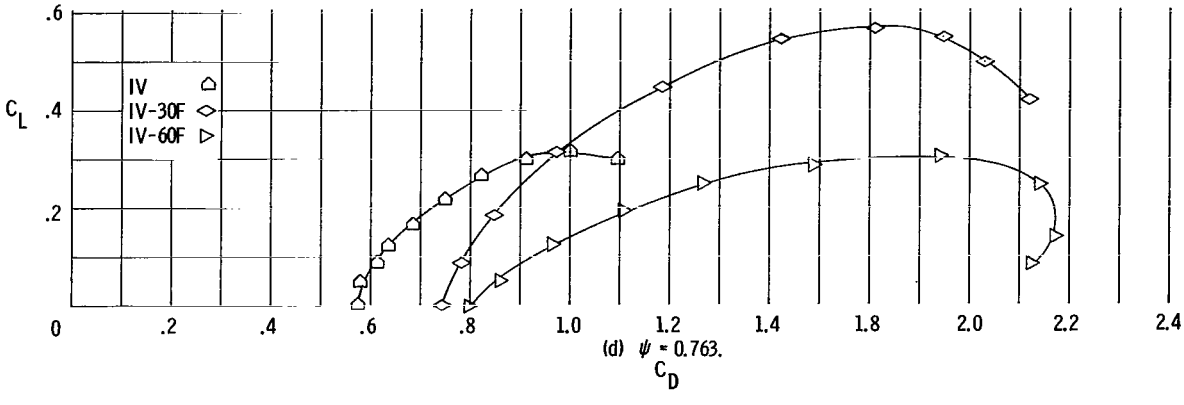

(d) ψ = 0.763.

Figure 9.- Concluded.

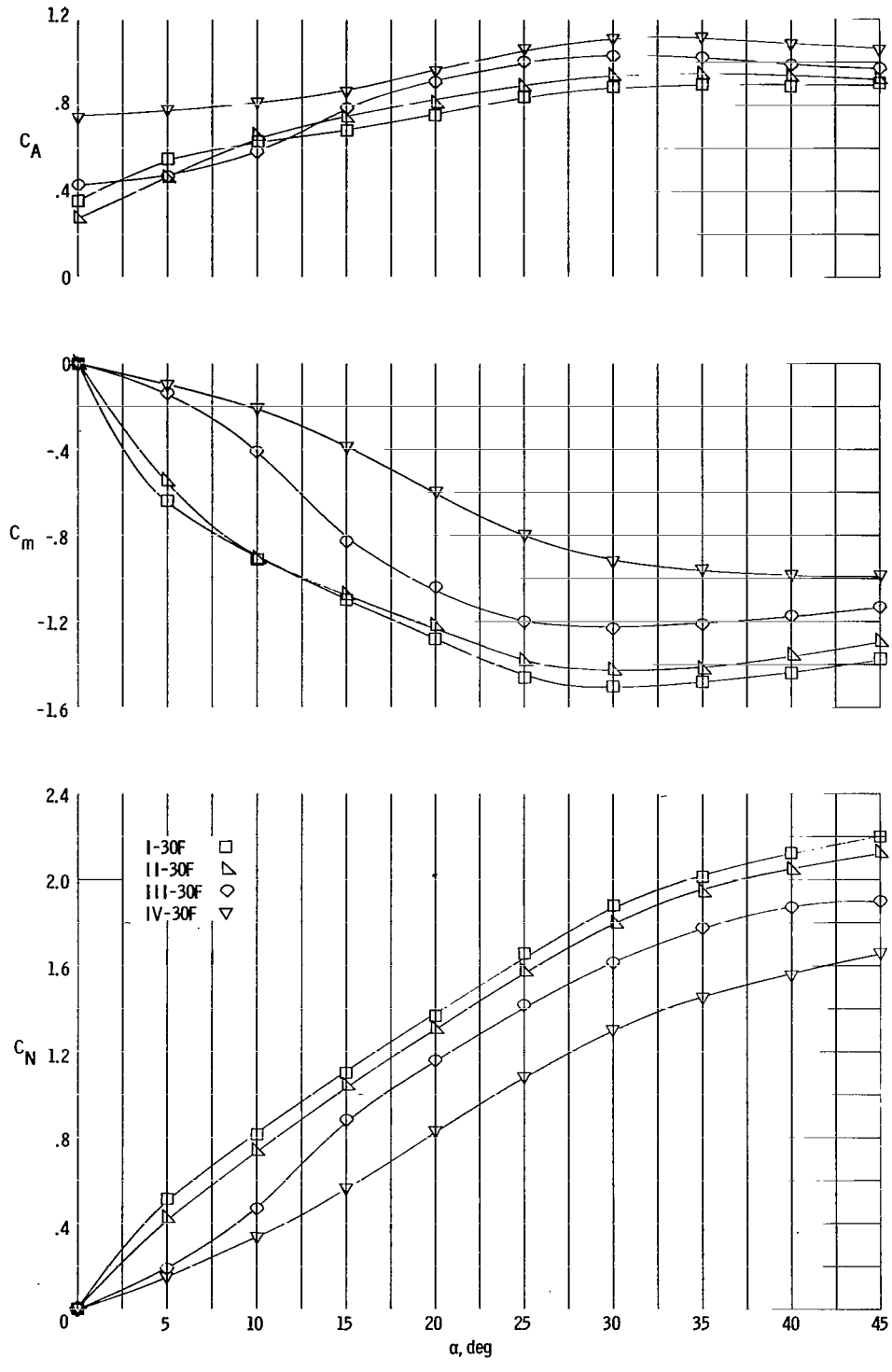

(a) 30^0 base flare.

Figure 10.- Effect of bluntness ratio for a given base flare on longitudinal force characteristics of a 10^0 semiapex-angle cone referred to body axis system. $M_\infty = 9.75$; $R = 1.56 \times 10^5$.

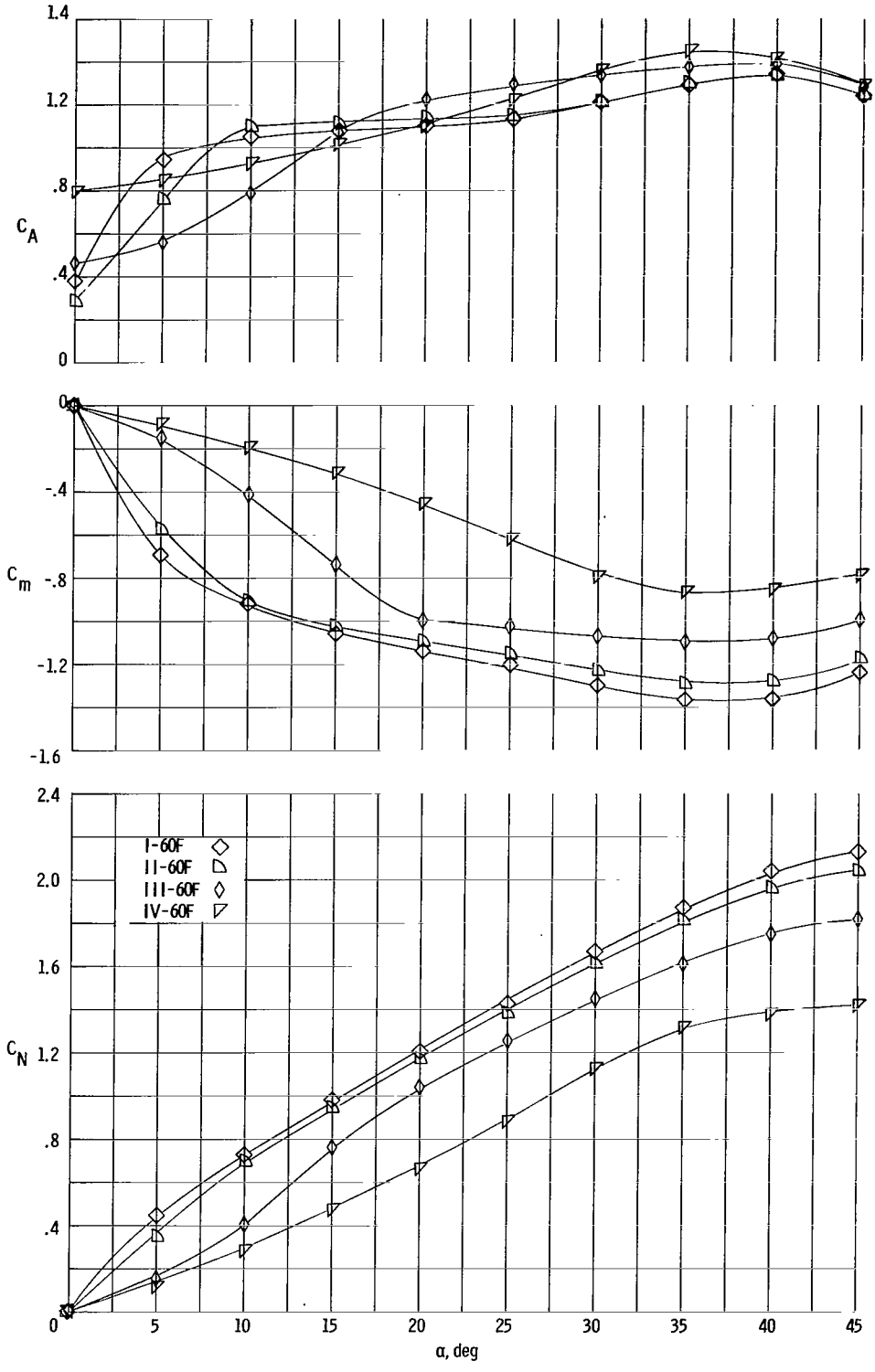

(b) 60^0 base flare.

Figure 10.- Concluded.

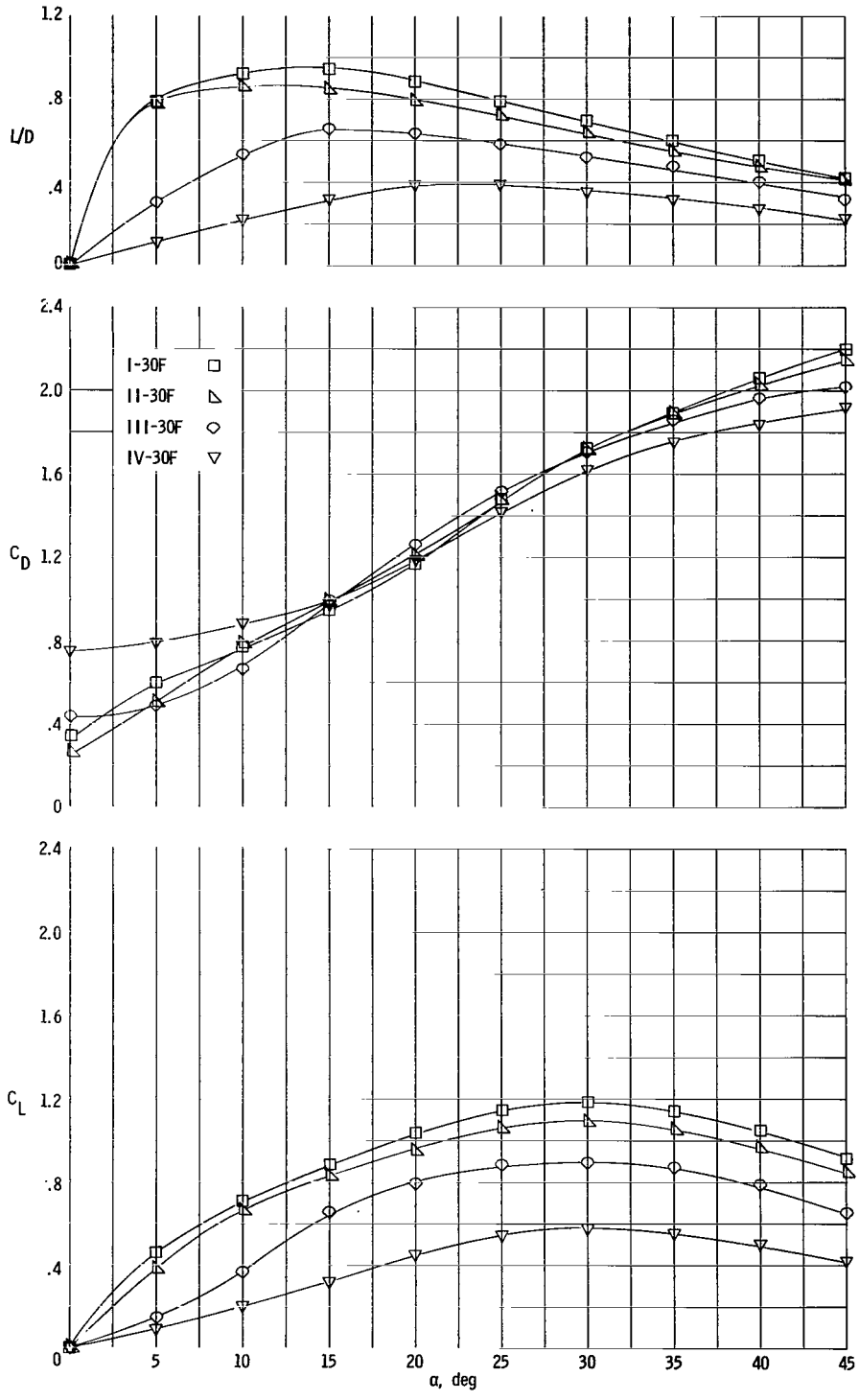

(a) 30^0 base flare.

Figure 11.- Effect of bluntness ratio for a given base flare on longitudinal force characteristics of a semiapex-angle cone referred to stability axis system. $M_\infty = 9.75$; $R = 1.56 \times 10^5$.

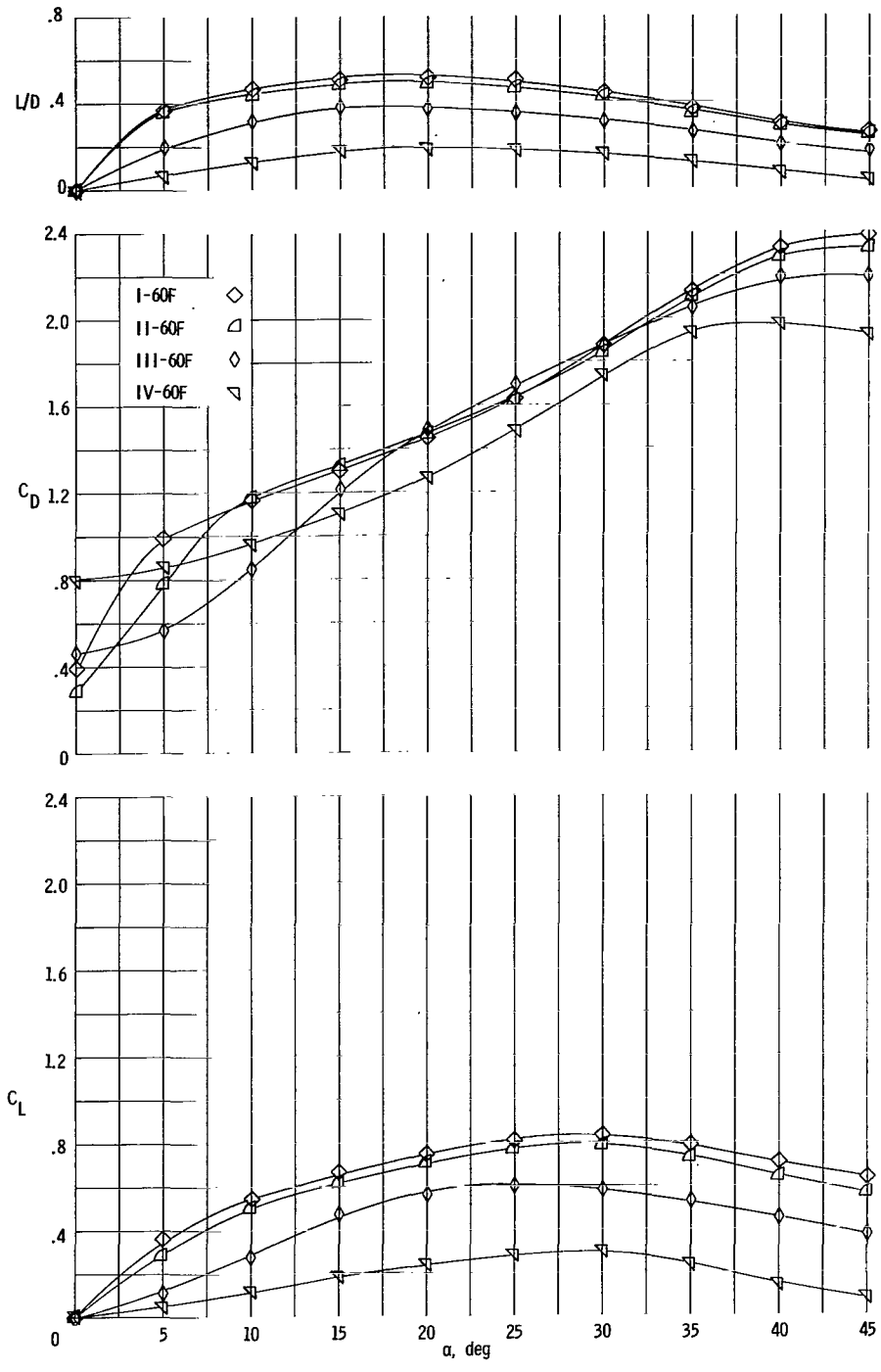

(b) 60^0 base flare.

Figure 11.- Concluded.

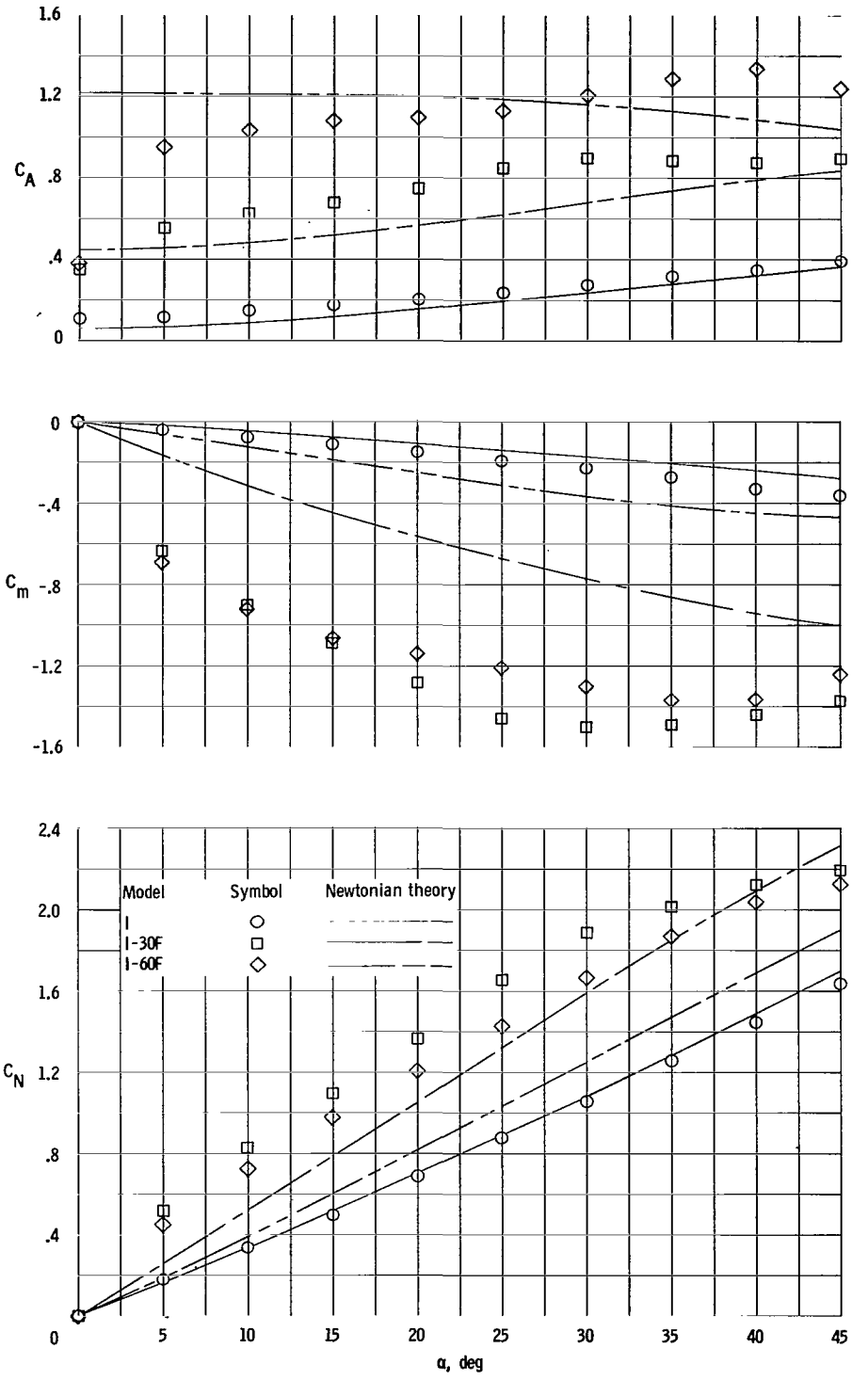

(a) $\psi = 0$.

Figure 12.- Comparison with theory of longitudinal force characteristics for a 10^0 semiapex-angle cone with various bluntness ratios and base flares. $M_\infty = 9.75$; $R = 1.56 \times 10^5$.

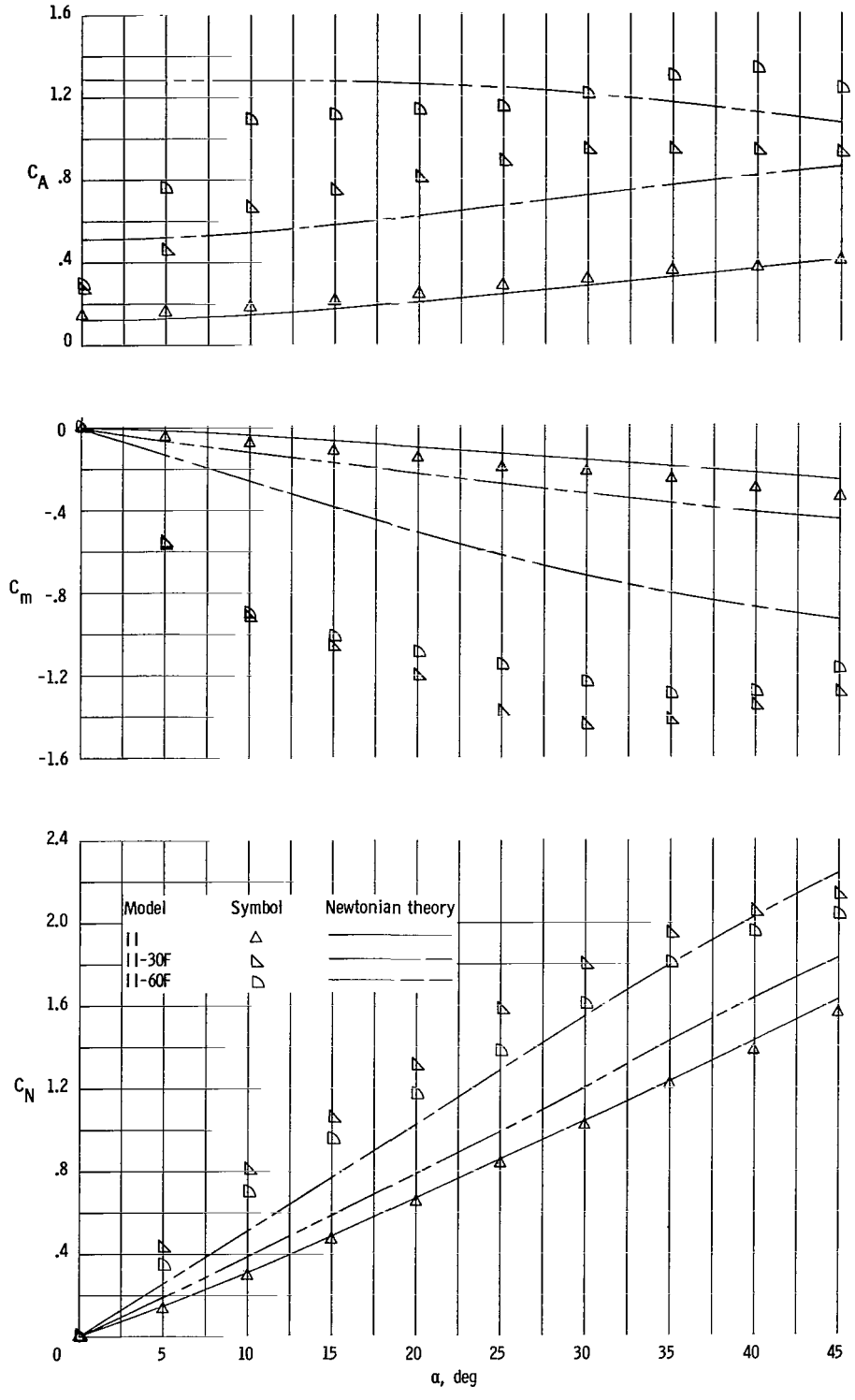

(b) $\psi = 0.255$.

Figure 12.- Continued.

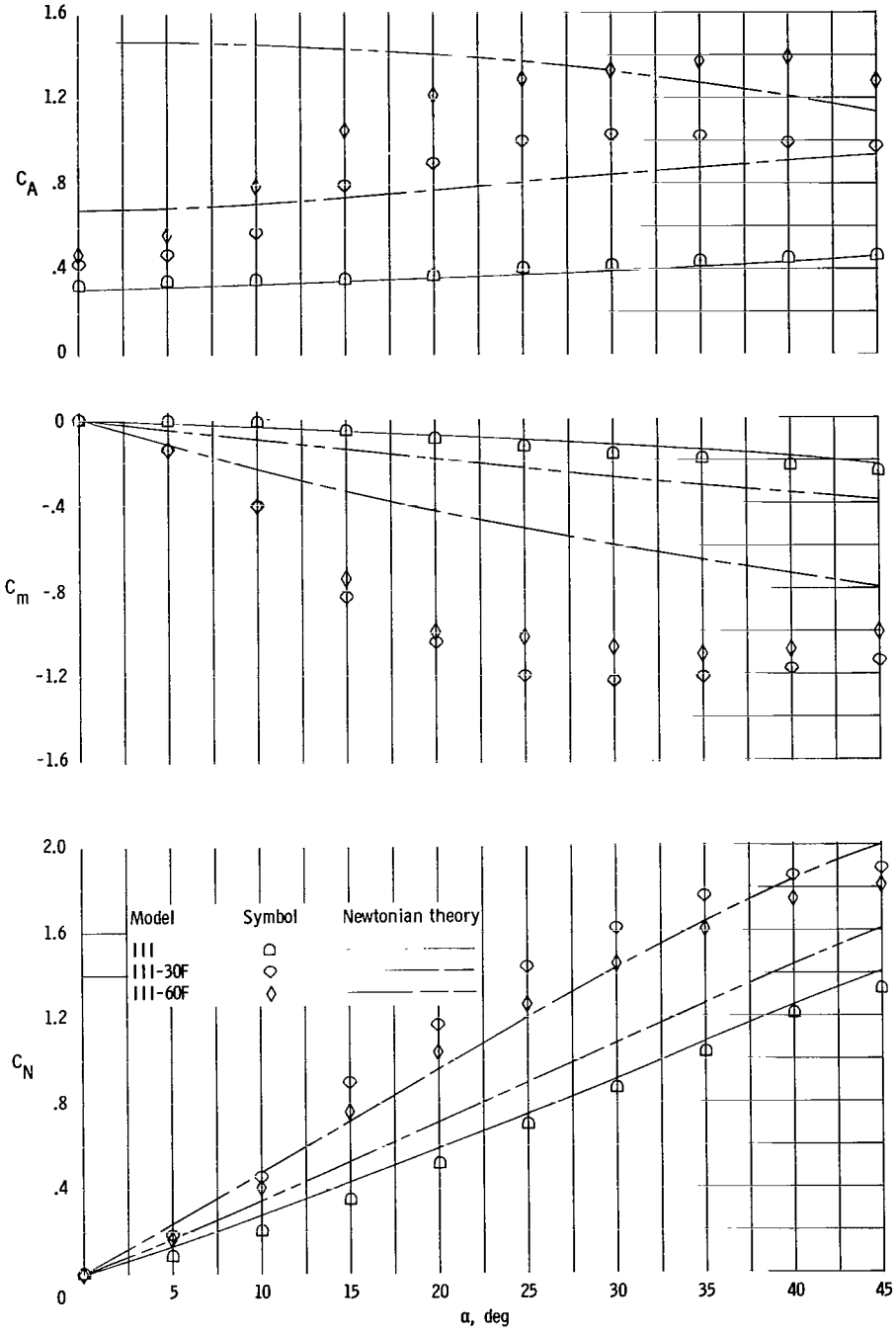

(c) $\psi = 0.509$.

Figure 12.- Continued.

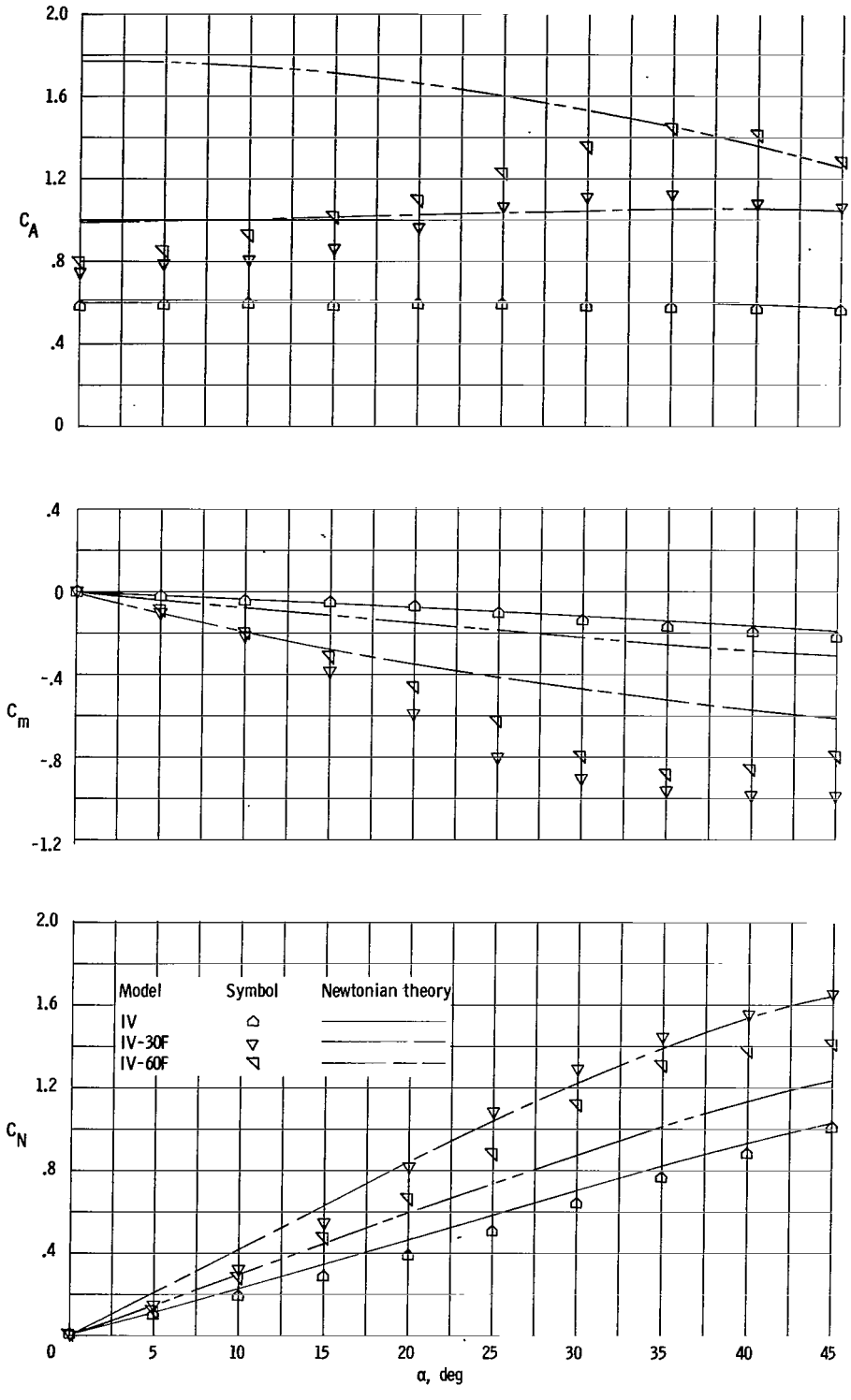

(d) $\psi = 0.763$.

Figure 12.- Concluded.

"The aeronautical and space activities of the United States shall be conducted so as to contribute . . . to the expansion of human knowledge of phenomena in the atmosphere and space. The Administration shall provide for the widest practicable and appropriate dissemination of information concerning its activities and the results thereof."

—NATIONAL AERONAUTICS AND SPACE ACT OF 1958

NASA SCIENTIFIC AND TECHNICAL PUBLICATIONS

TECHNICAL REPORTS: Scientific and technical information considered important, complete, and a lasting contribution to existing knowledge.

TECHNICAL NOTES: Information less broad in scope but nevertheless of importance as a contribution to existing knowledge.

TECHNICAL MEMORANDUMS: Information receiving limited distribution because of preliminary data, security classification, or other reasons.

CONTRACTOR REPORTS: Technical information generated in connection with a NASA contract or grant and released under NASA auspices.

TECHNICAL TRANSLATIONS: Information published in a foreign language considered to merit NASA distribution in English.

TECHNICAL REPRINTS: Information derived from NASA activities and initially published in the form of journal articles.

SPECIAL PUBLICATIONS: Information derived from or of value to NASA activities but not necessarily reporting the results of individual NASA-programmed scientific efforts. Publications include conference proceedings, monographs, data compilations, handbooks, sourcebooks, and special bibliographies.

Details on the availability of these publications may be obtained from:

SCIENTIFIC AND TECHNICAL INFORMATION DIVISION

NATIONAL AERONAUTICS AND SPACE ADMINISTRATION

Washington, D.C. 20546